



Intratumoral delivery of Mitomycin C using bio-responsive Gellan Gum Nanogel: In-vitro evaluation and enhanced chemotherapeutic efficacy

Nikhil Rai ^{a,b}, Disha Marwaha ^{a,b}, Shalini Gautam ^{a,b}, Ravi Prakash Shukla ^a, Madhu Sharma ^a, Neha Singh ^a, Pratiksha Tiwari ^a, Sandeep Urandur ^a, Venkatesh Banala Teja ^a, Sachin Nasik Sanap ^a, Krishna Yadav ^a, Avijit Kumar Bakshi ^a, Prabhat Ranjan Mishra ^{a,b,*}

^a Division of Pharmaceutics and Pharmacokinetics, CSIR-Central Drug Research Institute, Lucknow 226031, India

^b Academy of Scientific and Innovative Research (AcSIR), Ghaziabad 201002, India



ARTICLE INFO

Keywords:

Gellan gum polysaccharide
Redox-responsive intratumoral nanogel
Anticancer therapy

ABSTRACT

Intratumoral drug delivery systems hold immense promise in overcoming the limitations of conventional IV chemotherapy, particularly in enhancing therapeutic efficacy and minimizing systemic side effects. In this study, we introduce a novel redox-responsive intratumoral nanogel system that combines the biocompatibility of natural polysaccharides with the tailored properties of synthetic polymers. The nanogel features a unique cross-linked architecture incorporating redox-sensitive segments, designed to leverage the elevated glutathione levels in the tumor microenvironment for controlled drug release. Synthesis was performed using a microwave-assisted free radical polymerization technique, which facilitated efficient and rapid cross-linking. A Quality by Design strategy was implemented to optimize key parameters, ensuring the nanogel's suitability for intratumoral delivery, including ideal injectability, viscosity, and drug release characteristics.

Mitomycin C (MMC), a chemotherapeutic agent effective against hypoxic tumor cells, was efficiently loaded within the cross-linked nanogel. Optimal stability and drug loading were achieved at a 2:1 nanogel/MMC ratio. The nanogel's structure and composition were confirmed using elemental analysis, FTIR, NMR spectroscopy, and XRD. Stability studies demonstrated its robustness in simulated physiological conditions. In vitro evaluations revealed enhanced cellular uptake of the MMC-loaded nanogel, leading to effective cell cycle arrest, mitochondrial membrane potential disruption, and apoptosis. Co-localization studies with Lysotracker Green, a lysosomal marker, revealed that the nanogels were trafficked to lysosomes. Pharmacokinetic analysis showed significantly reduced systemic exposure (lower plasma Cmax) compared to intravenous administration, while biodistribution studies using IVIS imaging demonstrated prolonged retention of the nanogel within tumor tissues. In vivo studies using a 4T1 xenograft mouse model highlighted the superior antitumor efficacy of the intratumoral nanogel system compared to free MMC. The nanogel treatment resulted in significant tumor volume reduction, minimal changes in body weight, and reduced lung metastasis, as confirmed by histological analysis (H&E staining). Ki67 and TUNEL assays of tumor tissues further substantiated the nanogel's ability to suppress proliferation and induce apoptosis. These outcomes directly correlate with our goal of using a redox responsive nanogel system to improve localized drug delivery and minimize systemic side effects. This biodegradable, redox-responsive polymer system represents a significant advance in nanomedicine, offering a promising platform for safe and effective localized cancer therapy.

1. Introduction

Breast cancer presents a seminal global health challenge, indecorously impacting women's health worldwide. World Health

Organization (WHO) comprehensive report estimated 2.3 million annual burden was reported among women worldwide in 2020 [1]. Accounting for around a quarter of all diagnosed cancer in females each year. Despite positive footsteps in treatment, breast cancer persists as

* Corresponding author at: AcSIR, Biological Sciences, Area Coordinator- Preclinical and Translational Research, Pharmaceutics & Pharmacokinetics Division, Pre-Clinical South, Lab # 002, CSIR-Central Drug Research Institute, Lucknow 226031, U.P., India.

E-mail address: prabhat_mishra@cdri.res.in (P.R. Mishra).

the leading cause of cancer-related mortality among women globally, overshadowing even lung cancer [2]. The gap in the current strategies necessitates exploring innovative therapeutic strategies that maximize treatment efficacy while minimizing collateral damage.

Systemic chemotherapy, though effective, often causes significant side effects due to its low accumulation in tumor tissue and its impact on healthy tissues that rapidly divide alongside cancer cells [3,4]. The widespread toxicity caused by systemic anticancer drugs necessitates alternative delivery methods that minimize collateral damage to healthy tissues thereby, enhancing drug efficacy and improving patient quality of life. Over recent decades, intratumoral (IT) delivery has emerged as a promising alternative to overcome these limitations [5]. This delivery method offers significant advantages over conventional intravenous (IV) chemotherapy by precisely targeting cancer cells and minimizing systemic exposure [6]. While IV administration introduces drugs directly into the bloodstream without initial tumor binding, potentially leading to unintended consequences and suboptimal efficacy, intratumoral therapy (ITS) provides a compelling alternative for targeted and localized drug delivery.

The unique characteristics of the breast cancer microenvironment make it an ideal hotspot for targeted therapies. One of the most notable features is the significantly higher concentration of glutathione (GSH) in cancer cells (about 2–10 mM) compared to the normal extracellular matrix (about 2–20 μM) [7]. This disparity creates a high redox potential which, when combined with other cellular changes, can serve as an ideal trigger for the targeted release of anticancer drugs into tumor cells. Recognizing these unique properties of tumor microenvironment, researchers have focused on developing stimuli-responsive nanocarriers with tailored structural and functional characteristics. These advanced systems are designed to release their payload selectively in response to pathological tissue changes, maximizing treatment efficacy and safety. This approach offers several potential benefits in cancer therapy, including reduced premature drug leakage, enhanced drug accumulation in tumor cells, and the ability to overcome multidrug resistance, a major challenge in chemotherapy. Furthermore, the reductive environment and lower oxygen levels characteristic of tumor tissues can be exploited to design smart nanogels that release their medicinal payload in response to specific tumor signals, such as hypoxia [8,9].

Contemporary studies have revealed, the potential of polysaccharide-based nanogels as a promising platform for localized drug delivery. The multifunctional groups inherent to the polysaccharide backbone facilitate facile chemical alterations, enabling the creation of diverse nanostructures with tailored properties [10,11]. These nanogels combine biocompatibility with controlled release properties, including high drug loading capacity, water affinity, large surface area, and good mechanical stability [12–14]. Among the various polysaccharides explored, Gellan Gum (GalG) has gained significant attention in drug delivery applications. This anionic water-soluble polysaccharide, composed of 1 M α-l-rhamnose, 2 M β-D-glucose, and 1 M β-D-glucuronate, offers favorable properties including high water solubility, biocompatibility, biodegradability, and mechanical and physicochemical properties [15]. Availability of reactive hydroxyl/carboxylic functionalities allows for easy chemical alterations enabling the creation of materials with desired properties [15,16]. GalG has been creatively adapted into various modified release formulations, including sustained, controlled, and targeted delivery systems, with the goal of improving both the absorption and therapeutic effects of drugs [17–19]. In addition to its structural similarities to glycosaminoglycans found in the extracellular matrix, this polysaccharide offers a promising approach for developing effective localized drug delivery systems and modulating the tumor microenvironment for improved cancer therapy. [20,21]

Mitomycin C (MMC) is a broad-spectrum antibiotic with potent anti-tumor efficacy against the wide range of tumors, including lungs and pancreas, etc. Its cytotoxic mechanism involves the generation of free radicals that induce DNA damage, leading to cancer cell apoptosis. [22] Despite being a potent cytotoxic agent, MMC's effectiveness has been

historically constrained by severe systemic side effects, including irreversible bone marrow damage and hematological toxicities coupled with rapid elimination from the body [22–24]. To address these challenges researchers have explored various delivery strategies, including the development of nano-carrier systems like MMC-PLGA nanoparticles, MMC-nanomicelles, MMC-mesoporous silica nanoparticles, MMC-quantum dots, etc. [25–29]. While MMC has been successfully employed in treating various cancers, researchers have also dedicated considerable efforts to investigating its potential application in breast cancer therapy [30,31]. Previous studies have highlighted MMC as a potential option for intratumoral delivery. Its reported properties, including hypoxia-dependent activation and cell cycle-independent cytotoxicity, make it particularly well-suited for targeting hypoxic cancer cells, a characteristic prevalent in many solid tumors, including breast cancer [23,32].

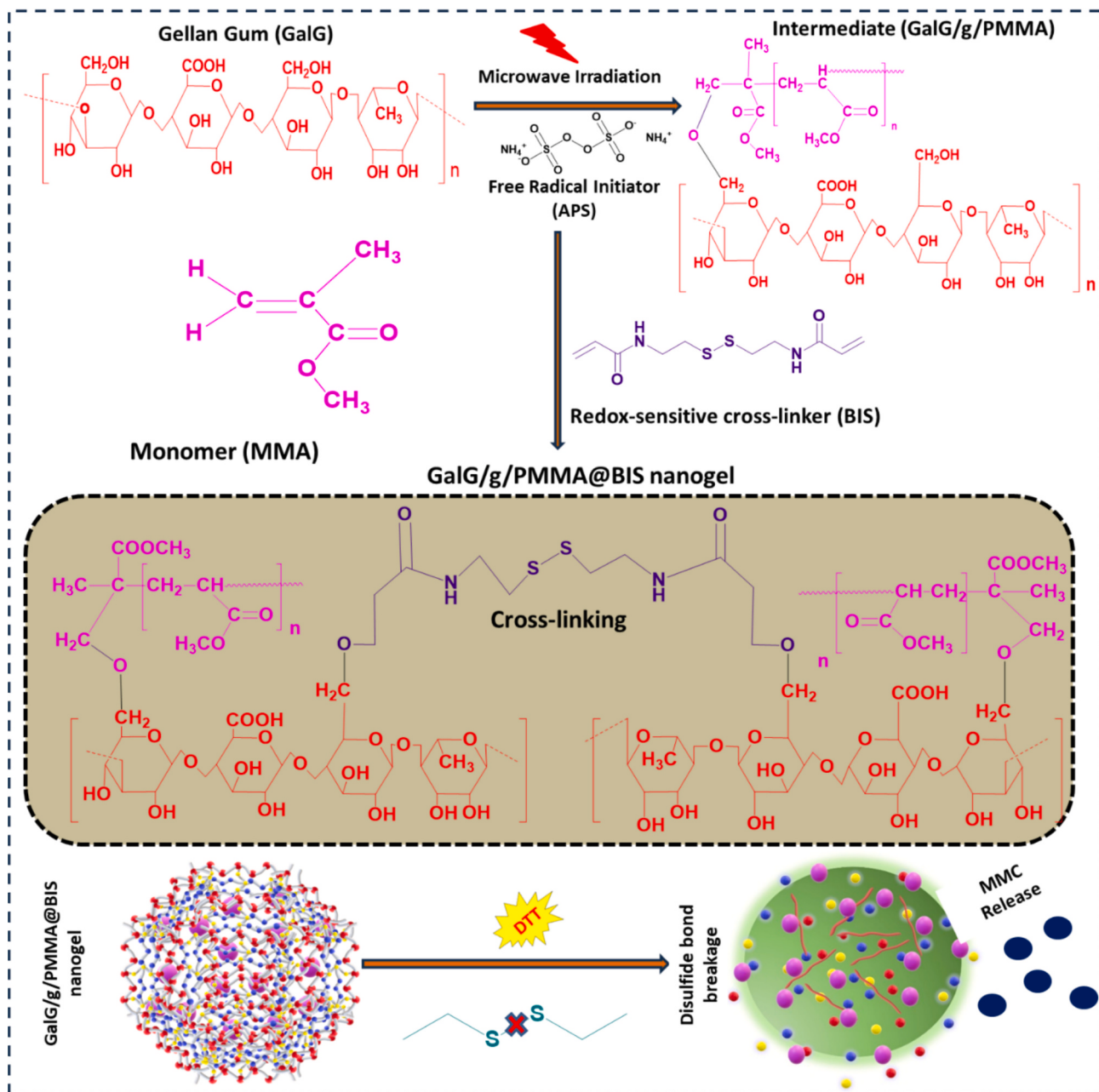
The tumor microenvironment, characterized by the presence of tumor stroma, high interspace fluid pressure, hypoxic conditions, and acidic pH, can create barriers to drug penetration within the tumor mass [32,33]. To address these issues, a hypoxic-responsive biodegradable nanogel could be a promising solution. Their unique properties, such as tunable size, surface modifications, hypoxic activation, and controlled drug release, can enhance drug delivery to the tumor microenvironment and improve intratumoral therapeutic efficacy. While natural polysaccharides possess low immunogenicity, their high viscosity and insufficient mechanical strength necessitate the inclusion of synthetic polymers. Crosslinking the combined polymers with a redox segment can address these limitations, enhance injectability and mechanical properties, and enable targeted and controlled drug release [10,34]. This approach holds promise for enhancing IT delivery while minimizing systemic leakage and toxicity.

To overcome these challenges, we have focused on developing a novel bio-reducible co-polymerized GalG nanogel (MMC-GalG/g/PMMA@BIS) for temporal and spatial delivery of MMC, intending to achieve improved therapeutic outcome in breast cancer therapy. Herein, the monomer methyl methacrylate (MMA) was allowed to polymerize and was subsequently cross-linked with GalG using redox responsive-N, N'-Bis (acryloyl) cystamine (BIS) to achieve redox-sensitive properties when exposed to intracellular GSH. This will in turn trigger the dismantling of nanogel structure enabling the release of MMC, hence facilitating efficient spatial intratumoral distribution with minimal systemic leakage. We have utilized synthetic monomers such as MMA to address the issues of high viscosity, drug release, and mechanical strength associated with GalG. This research holds substantial potential for enhancing breast cancer treatment outcomes. By harnessing the distinctive properties of both MMC and smart nanogels, we strive to create a more effective and tolerable therapy that reduces systemic toxicity and maximizes anti-tumor efficacy. **Scheme 1** represents the preparation of GalG/g/PMMA@BIS nanogel via crosslinking through redox-sensitive N, N'-Bis (acryloyl) cystamine (BIS).

2. Materials and methodology

2.1. Materials

Gellan gum (>92 % 500kD), an anionic-tetra polysaccharide fermentation product from *Spingomonas elodea* bacterium, was obtained from Sigma-Aldrich® Solutions (Phytigel™). The Gellan gum used in this study was used without further purification. Mitomycin C (98 %, 334.33 g/mol), and ammonium persulfate (APS) were purchased from Millipore Sigma Aldrich. *N, N*-Bis(acryloyl) cystamine (BIS), and methyl methacrylate (MMA) were procured from Supelco® Solutions. Ethanol, PBS, and propidium iodide (PI) were supplied by the Tokyo Chemical Industry (TCI). RPMI-1640 medium, fetal-bovine serum (FBS), trypsin (0.25 %)-EDTA (1×), and antibiotic/antimycotic solution (100×) were obtained from Gibco®/Invitrogen™ (Thermo Fisher Scientific-Life Technologies, USA). Whereas, cationic carbocyanine dye



Scheme 1. Diagram showing the preparation of cross-linked redox-responsive GalG/g/PMMA@BIS nanogel using microwave irradiation. In a reductive environment (DTT), the nanogel degrades due to cleavage of disulfide bonds, leading to the release of the encapsulated drug (MMC).

(JC – 1), phenylindole nucleus-staining dye (DAPI), dichlorodihydro-fluorescein diacetate-ROS sensitive dye (DCFDA), and MTT were purchased from MP Biotech (Madhya Pradesh, India), and the annexin-V labeled FITC/PI apoptosis kit was procured from BD Pharmingen™ (USA). RP-HPLC/LC-MS/MS grade solvents and reagents (MeOH and ACN) were from Sigma-Aldrich® (Merck, India). Triple-distilled water (TDW) was taken up from the in-house Milli-Q system (Millipore, Bedford, USA). Additional analytical/bioanalytical-grade reagents were obtained from various chemical vendors.

2.2. Methodology

2.2.1. Preparation of Redox Responsive Cross-linked Gellan Gum Nanogel (GalG/g/PMMA@BIS Nanogel)

The cross-linked nanogel (GalG/g/PMMA@BIS nanogel) was prepared using an electromagnetic irradiation-induced free radical

polymerization process, offering rapid reaction times and enhanced control over particle size distribution [35,36]. The procedure begins with the careful preparation of a reaction mixture containing precisely measured quantities (Table S1) of gellan gum (GalG), methyl methacrylate (MMA), and *N,N*-Bis(acryloyl) cystamine (BIS) dissolved in 200 mL of double-distilled water. This solution was maintained at 50 °C under constant stirring to ensure complete dissolution. Ammonium persulfate (APS) was used as the redox initiator, generating free radicals under mild conditions to promote efficient polymerization while minimizing the potential degradation of sensitive components.

The reaction mixture was subjected to four cycles of microwave exposure, each lasting 40 s, followed by rapid cooling in an ice bath. This cyclic heating and cooling approach offers precise control over reaction kinetics, prevents unwanted side reactions, and significantly reduces overall reaction time compared to conventional heating methods. Following microwave-assisted polymerization, the resulting solution

was cooled to room temperature and precipitated in excess methanol to remove unreacted monomers and initiator residues. It was left undisturbed overnight. The resulting nanogel was then separated by filtration, washed with methanol, and dried in a hot air oven at 50 °C for 12 h. To enhance the functionality of our nanogel, we perform an alkaline hydrolysis step using 1 M NaOH at 75 °C for 1 h. This treatment partially hydrolyzes the PMMA component, introducing carboxylic acid moieties that improve the hydrophilicity and drug-loading capacity of the nanogel [37]. A critical aspect of our purification process involves the removal of any residual PMMA homopolymer using a solvent extraction technique with a mixture of ethyl acetate and methanol (50:50) [38]. This step ensures the purity of our final product, crucial for its intended biomedical applications. The percentage grafting efficiency (%GE) of GalG/g/PMMA@BIS nanogel was evaluated by the following equation,

$$\%GE = \frac{((\text{Weight of GalG/g/PMMA@BIS nanogel}) - \text{Weight of GalG})}{\text{Weight of MMA}} \times 100 \quad (1)$$

The GalG/g/PMMA@BIS nanogel thus obtained was subsequently loaded with MMC using nanogel/MMC ratios at 2:1 that yielded the most optimal balance between drug loading efficiency and nanogel stability. The incorporation of BIS as a cross-linker introduces a redox-responsive segment within GalG/g/PMMA@BIS nanogel, allowing for targeted drug release in the reductive tumor microenvironment. The presence of both hydrophilic (GalG) and hydrophobic (PMMA) components, creates a versatile structure suitable for various therapeutic payloads. Moreover, microwave-assisted synthesis offers significant advantages in terms of reaction speed and reproducibility, which are crucial factors when considering future manufacturing processes.

2.2.2. Optimization of MMC loading in GalG/g/PMMA@BIS (MMC-GalG/g/PMMA@BIS) nanogel

The MMC loading in GalG/g/PMMA@BIS nanogel was optimized to achieve efficient delivery of the therapeutic agent (MMC). Briefly, 10 mg/mL of GalG/g/PMMA@BIS nanogel solutions in water were incubated with 2.5, 5, and 10 mg/mL solution of MMC to obtain a nanogel/drug ratio of 4:1, 2:1, and 1:1 respectively. The final working volume was adjusted upto 5 mL, and left for incubation at controlled room condition (25 °C, 12 h, 50 rpm). Following confirmation of complete mixing and successful drug loading, MMC-loaded nanogel (MMC-GalG/g/PMMA@BIS nanogel) was subjected to centrifugal separation at 2500 rpm. Drug loading (MMC) and entrapment efficiency (MMC) were determined using a previously described method [39]. The absorbance of the MMC in the supernatant was measured at λ_{max} of 365 nm, and its concentration was determined by interpolating the calibration curve in the MMC concentration range of 0.20–6.40 µg/mL ($R^2 = 0.999$ and $y = 0.1437x + 0.0029$).

$$\%DL = \frac{(\text{Total amount of MMC} - \text{Free MMC})}{\text{Amount of MMC loaded nanogel}} \times 100 \quad (2)$$

$$\%EE = \frac{(\text{Total amount of MMC} - \text{Free MMC})}{\text{Amount of MMC in nanogel}} \times 100 \quad (3)$$

2.2.3. Optimization of Redox Responsive Cross-linked nanogel (GalG/g/PMMA@BIS nanogel) using Box-Behnken design

To optimize MMC-GalG/g/PMMA@BIS nanogel formulation, we employed a sophisticated Box-Behnken design (BBD) within the framework of Response Surface Methodology (RSM). This approach allowed us to efficiently explore the multidimensional parameter space within a minimal number of experimental runs, providing valuable insights into the complex relationships between formulation variables and nanogel characteristics. Response surface (3D) and contour plot (2D) graphical visualization methods were used to explore the correlation between responses and independent variables including their interaction types

[40,41].

The initial trial experiments led to optimization of different factors, like; Factor A (Amount of GalG), Factor B (Amount of MMA/N, N BIS Cyst), and Factor C (Amount of APS) are the critical process variables that influence the responses like percentage grafting efficiency (%GE), particle size (PS), zeta potential (ZP), and percentage entrapment efficiency (%EE). These factors were systematically varied across low (-1) and high (+1) levels as represented in Table 1. A total of fourteen possible independent experiments (F1–F14) including two center points were carried out based on a selected range (Table S1) using Design-Expert® 11.1.2.0 software (Trial version, Stat-Ease, Inc., Minneapolis, USA). The ranges were chosen to provide adequate variability to study the effects of formulation variables on the nanogel's properties, enabling identification of an optimal level that ensures effective polymerization, nanoscale particle size, and suitable injectability. A low polymer concentration range of 200–500 mg was selected to ensure optimal injectability and nanoscale size. A balanced ratio of MMA/N, N BIS acrylamide was crucial to maintain nanogel stability and drug release properties, while a moderate APS concentration facilitated controlled polymerization and nanogel formation. The experiments were performed using various combinations of independent variables, and the obtained data were compared with predicted values for model validation.

The analysis of variance (ANOVA) method was concluded, and the predicted- R^2 and adjusted- R^2 values were used to assess the model fit and prediction performance. A confidence level (95 %) was adopted to determine the precision of model prediction and the p -values ≤ 0.05 were acknowledged as significant [40]. The optimization of the desired quality GalG/g/PMMA@BIS nanogel was achieved by evaluating the overall numerical desirability function.

The optimized formulation with highest overall desirability was obtained with the help of numerical optimization using design expert software. The formulation with optimized levels of the factors i.e. A (Amount of GalG), B (Amount of MMA/N, N BIS-Cyst), and C (Amount of APS) was prepared similarly as discussed in the Section 2.2.1.

2.2.4. Evaluation of GalG/g/PMMA@BIS nanogel

2.2.4.1. Characterization of GalG/g/PMMA@BIS nanogel. To justify the successful synthesis of cross-linked GalG/g/PMMA@BIS nanogel we employed a comprehensive suite of analytical techniques. This multi-faceted approach provided detailed insights into the chemical composition, molecular structure, and elemental makeup of our nanogel

Table 1

Independent variables are labeled along with the constraints and goals of dependent Variables (Variables selected for BBD optimization).

Independent variables	Level				Mean
	Minimum	Coded Low	Maximum	Coded High	
A: Amount of GalG (mg)	200.00	-1 ↔ 200.00	500.00	+1 ↔ 500.00	350.00
B: Amount of MMA/N, N BIS Cyst (mg)	50.00	-1 ↔ 50.00	350.00	+1 ↔ 350.00	200.00
C: Amount of APS (mg)	5.00	-1 ↔ 5.00	15.00	+1 ↔ 15.00	10.00

Dependent variables	Minimum	Maximum	Mean	Constraints/Goal
R1: GE (%)	89.3	98.2	93.71	Maximize
R2: PS (nm)	103.7	157.2	127.48	Minimize
R3: PDI (-)	0.11	0.26	0.196	Minimize
R4: ZP (mV)	-34	-23	-27.49	Maximize
R5: EE (%)	90.01	97.87	93.03	Maximize

Note: * (GE) Grafting Efficiency, (PS) Particle Size, (PDI) Polydispersity Index, (ZP) Zeta Potential, and (EE) Entrapment Efficiency.

system.

Fourier-transform infrared (FTIR) spectroscopy served as our initial analytical tool, offering a broad overview of the functional groups present in the nanogel structure. Samples (GalG/g/PMMA@BIS nanogel, GalG, and MMA) were analyzed by FTIR spectroscopy (PerkinElmer-Spectrum II FT-IR Spectrometer, Norwalk, CT, United States) across the spectrum ranging from 4000 to 400 cm⁻¹ [42]. This analysis allowed us to identify key functional groups characteristic of our copolymer components, including the carboxyl and hydroxyl groups of gellan gum, and PMMA, and the amide bonds of the BIS crosslinker.

To further corroborate our FTIR findings, we have carried out proton nuclear magnetic resonance (¹H NMR) spectroscopy. This offered insights into the molecular environment of adjacent hydrogen atoms within our nanogel structure. The samples of GalG, MMA, and the final GalG/g/PMMA@BIS nanogel were prepared in appropriate deuterated solvents (D₂O, CDCl₃, and DMSO-d₆, respectively) to ensure optimal spectral resolution. The NMR spectrum of GalG, MMA, and GalG/g/PMMA@BIS nanogel were acquired at room temperature using a high-field 400 MHz-NMR spectrophotometer (Agilent Technologies, Santa Clara, CA, USA) [33].

The elemental composition (hydrogen, carbon, and nitrogen) of GalG, MMA, and GalG/g/PMMA@BIS nanogel was performed by an elemental analyzer (EuroVector instrument with 0.1 to 1 µg of detection limit). A standard reference material, acetanilide, was used for calibration. After calibration, 1–2 mg samples were placed in an auto-sampler, where the sample was combusted at a temperature of approximately 980 °C. This high-temperature combustion process converted the elements of interest (C, N, and H) into their respective gaseous products. The resulting eluted gases were analyzed by Callidus 5.0. software [43].

X-ray diffraction (XRD) analysis was performed to investigate the crystalline or amorphous nature of the GalG, PMMA, and GalG/g/PMMA@BIS nanogel. The samples were scanned over a 2θ range of 5° to 60° at a scan rate of 2°/min, operating at a voltage of 9 kV and a current of 30 mA (Rigaku, Japan; SmartLab software). The diffraction patterns obtained were used to identify structural differences among the samples. Characteristic peaks were analyzed to evaluate changes in crystallinity following cross-linking compared to the native gum (GalG) and PMMA [44].

Combinations of these complementary analytical techniques – FTIR, ¹H NMR, elemental analysis, and XRD – provided a comprehensive structural characterization of our GalG/g/PMMA@BIS nanogel.

2.2.4.2. Particle size, PDI, and Zeta Potential. Our comprehensive characterization of the MMC-GalG/g/PMMA and MMC-GalG/g/PMMA@BIS nanogels employed a suite of advanced analytical techniques to elucidate their physicochemical properties and morphological features. This multi-faceted approach provided crucial insights into the nanogel structure and behavior, essential for optimizing their performance as drug delivery systems. We investigated the particle size, distribution (PDI), and surface zeta potential using dynamic light scattering (DLS) with a Malvern Zetasizer (Nano-Zs 2000, Malvern Panalytical Instruments, U.K.). Samples were carefully diluted threefold with triple-distilled water to ensure optimal measurement conditions [7]. Each measurement was repeated three times to ensure statistical robustness and reliability of the data.

2.2.4.3. Morphological characterization. To complement the DLS data and gain direct visual insights into nanogel morphology, we employed a trio of high-resolution imaging techniques: transmission electron microscopy (TEM), scanning electron microscopy (SEM), and atomic force microscopy (AFM).

Electron microscopy (SEM and TEM) and atomic force microscopy (AFM) techniques were implemented to investigate the morphology of the MMC-GalG/g/PMMA@BIS nanogel. For the TEM examination, nanogel formulation was coated onto a copper grid and allowed to settle

for 15 min. Negative staining was applied using a 4 % (w/v) tungstophosphoric acid solution [7]. The samples were air-dried at ambient temperature before imaging by TEM (JEM1400; Tokyo, Japan). Additionally, the SEM analysis was conducted by scanning formulations, (MMC-GalG/g/PMMA, and MMC-GalG/g/PMMA@BIS nanogel) at a 2.0 kV acceleration voltage (Carl Zeiss EVO40, FEI Quanta 250 SEM) [45]. This comparative analysis allowed us to directly observe the impact of BIS crosslinking on nanogel morphology, providing valuable insights into the structural changes induced by our synthesis process. Moreover, the developed formulation (MMC-GalG/g/PMMA@BIS nanogel) was also subjected to topographical and morphological scanning using TriA-AFM/SPM (A.P.E.R, Italy) performed with a tapping mode. A cantilever (40 N/m, NSC15/AI BS) with dimensions of length 125 µm, width 30 µm, and tip thickness of 4 µm was utilized for scanning across the sample [39]. The resulting AFM images offered unique insights into the surface texture and nanoscale features of our MMC-GalG/g/PMMA@BIS nanogels.

2.2.4.4. Redox susceptibility study. To evaluate the nanogel's behavior in a reductive environment, we employed dynamic light scattering (DLS) technique, simulating physiological conditions that might be encountered *in vivo*. The experimental design focused on monitoring hydrodynamic and morphological changes to the reductive environment (10 mM DTT; dithiothreitol), which were monitored by the DLS and TEM techniques, respectively [7,33]. By tracking alterations in particle size, PDI, and morphology over a 24-hour period, the study aimed to elucidate the nanogel's structural stability and its potential for triggered disassembly or cargo release in response to reductive stimuli. This approach offers several advantages for understanding the nanogel's behavior.

2.2.4.5. In-vitro MMC release. In our investigation of the drug release behavior of the optimized nanogel formulations, we employed a comprehensive approach to elucidate the complex interplay between nanogel structure, drug payload, and environmental factors (10 mM DTT, added in PBS, and plasma) influencing release profiles. A control experiment was also conducted under non-reductive conditions, using nanogels without DTT, to assess the release behavior in the absence of a reductive environment.

In-vitro MMC release/dissolution from MMC-GalG/g/PMMA and MMC-GalG/g/PMMA@BIS nanogel was conducted by dialysis bag method. A dialysis bag was used to retain the formulation and allow the release of the drug into the release media [7]. The release study was conducted in reductive (10 mM DTT), which is the hallmark of the tumor microenvironment [33,46]. To simulate physiological conditions and evaluate the potential *in-vivo* performance, the experiment was also conducted in the simulated physiological fluids (25 % plasma added with 10 mM DTT). The drug release in simulated physiological fluids (25 % plasma in PBS/DTT) provides insight into how blood components might influence drug release behavior under conditions closer to those experienced in the tumor vicinity and body [28].

Briefly, two milliliters of MMC-GalG/g/PMMA and MMC-GalG/g/PMMA@BIS nanogel solution were transferred to the dialysis bag. The system was kept in a magnetic stirrer under controlled conditions (100 rpm at 37 °C). One milliliter sample was withdrawn at predetermined time intervals (0, 2, 4, 6, 8, 12, 16, 24, 48, and 72 h) and simultaneously one milliliter of respected (PBS and 25 % plasma in PBS with 10 mM DTT) media was added to ensure the simulated sink condition. A time-course analysis, of MMC in each sample was performed by our RP-HPLC system (Shimadzu, Japan). The percent of release was plotted against time for every sample. Further In-vitro drug release was fitted into Zero-order, Higuchi, first-order, and Korsmeyer-Peppas models to determine the drug release kinetics from the developed formulation. (A detailed HPLC method is described in Supplementary Information 2.1.)

2.2.4.6. Storage and serum stability study. In our comprehensive evaluation of the MMC-GalG/g/PMMA@BIS nanogel system, we conducted a rigorous storage stability study to assess its long-term viability under different temperature conditions. We stored nanogel samples at 4 °C and 25 °C for eight weeks, systematically examining them at predetermined intervals. Our analysis focused on three critical parameters: particle size, PDI, and EE.

The prototype MMC-GalG/g/PMMA@BIS nanogel was also incubated with 10 % fetal bovine serum (FBS) and a 0.25 % NaCl solution to simulate physiological conditions. The study was conducted to assess the impact of serum proteins and ionic strength on the stability of the nanogel, specifically regarding its particle size and polydispersity index (PDI) [39]. These metrics provided us with valuable insights into the nanogel's physical stability and its ability to retain the encapsulated drug over time [47].

2.2.4.7. Rheological measurements. The rheological properties of the MMC-GalG/g/PMMA and MMC-GalG/g/PMMA@BIS nanogel were studied using an Anton-Paar rheometer RH92, equipped with cone (1° cone angle) and plate (60 mm diameter) geometries. The viscosity vs Shear rate was measured at a constant frequency. All rheological properties were analyzed using RheoCompass software [48].

2.2.5. Evaluation of in-vitro cellular activity

To complement our physicochemical characterization, we initiated a series of in vitro cellular studies to evaluate the biological activity and potential efficacy of our nanogel formulation. All cell-based study was performed on MDA-MB-231 cells, a proven model for triple-negative breast cancer (TNBC), procured from the inhouse CDRI facility, cultured in DMEM (Dulbecco's Modified Eagle Medium) supplemented with 10 % FBS, 2 mM glutamine, antibiotics (100 mg/mL), and NEAA (1 % -non-essential amino acids). Cells were maintained in a controlled environmental incubator at 37 °C with 5 % CO₂ to ensure optimal growth and confluence.

In our comprehensive evaluation of the MMC-GalG/g/PMMA, and MMC-GalG/g/PMMA@BIS nanogel system's efficacy against triple-negative breast cancer, we conducted a series of in vitro cellular studies using the MDA-MB-231 cell line. Our experimental approach encompassed multiple assays to assess various aspects of the nanogel's interaction with cancer cells and its therapeutic potential. Throughout our studies, we maintained rigorous experimental controls and performed each assay in triplicate to ensure the reliability and reproducibility of our results. A detailed specification of each cell-based study has been provided in the supplementary Section 2.3.

2.2.5.1. Cell viability assay. The MTT assay was performed to evaluate the cytotoxic effects of the MMC loaded formulations on both cancerous (MDA-MB-231) and non-cancerous (HEK-293) cell lines, with the addition of HEK 293 cell lines to confirm the specificity of the nanogel's action. MDA-MB-231 and HEK-293 cells were cultured in DMEM supplemented with 10 % FBS and 1 % penicillin-streptomycin in a 37 °C incubator with 5 % CO₂. Cells were seeded into 96-well plates at a density of 3×10^3 cells/well (80–90 % confluence) and allowed to adhere overnight. Following cell attachment, the formulations were diluted to various concentrations (MMC concentrations equivalent to 0–50 μM, and 0–40 μM in MDA MB 231, and HEK 293 cells respectively in fresh medium and added to the cells in triplicate wells for each concentration. Cells treated with blank nanogel (without drug) served as controls. After 24 h of incubation, cell viability was assessed by adding 10 μL of MTT solution (5 mg/mL in PBS) to each well and incubating for 4 h. Subsequently, the medium was removed, and 100 μL of DMSO was added to dissolve the formazan crystals. Absorbance was measured at 570 nm using a microplate reader. This allowed us to calculate IC₅₀ values and compare the efficacy of our nanogel formulations to free MMC.

2.2.5.2. Cell uptake studies. Building on the findings from the cytotoxicity study, we next investigated the cellular uptake studies to understand its internalization of developed nanogel and interaction with cells. For experimental purposes, cells were seeded at a density of 1×10^3 cells/well onto poly-L-lysine-coated coverslips placed within 6-well plates. Experiments were initiated upon reaching 80–90 % cell confluence. We encapsulated Coumarin-6 (C-6), a fluorescent probe, in our nanogels (C6-GalG/g/PMMA, and C6-GalG/g/PMMA@BIS) and used confocal laser scanning microscopy (CLSM) to visualize their intracellular localization. Complementing this qualitative analysis, we also performed quantitative uptake measurements using flow cytometry. These studies allowed us to compare the cellular internalization of different nanogel formulations and assess their potential for efficient drug delivery.

2.2.5.3. Cell cycle arrest analysis. To elucidate the mechanism of action of our MMC-GalG/g/PMMA, and MMC-GalG/g/PMMA@BIS nanogel, we investigated their effects on the cell cycle progression. Prior to the study, cells were seeded at a density of 1×10^3 cells/well in six-well plates and incubated for 24 h to achieve 80–90 % confluence. Using propidium iodide staining and flow cytometry tools, we analyzed the distribution of cells in different phases of the cell cycle following treatment. This analysis provided insights into whether our formulations induced cell cycle arrest, and if it does then at what stage ensuring a common mechanism of action for many anticancer drugs.

2.2.5.4. Mitochondrial membrane potential (MMP) assay. We also assessed the impact of our treatments on mitochondrial function, a key indicator of cellular health and apoptosis initiation. MDA-MB 231 cells were cultured at a density of 1×10^5 cells/well in 12-well plates under standard conditions for 24 h to establish a confluent monolayer. Using the JC-1, a cationic green fluorescent dye, 5,5',6,6'-tetrachloro-1,1',3,3'-tetraethylbenzimidazolocarbocyanine iodide, we measured changes in mitochondrial membrane potential (MMP) following exposure to free MMC, MMC-GalG/g/PMMA, and MMC-GalG/g/PMMA@BIS nanogel. This assay allowed us to detect early signs of apoptosis and compare the potency of our nanogels to free MMC in inducing mitochondrial dysfunction.

2.2.5.5. Apoptosis. To quantify the apoptotic cell population MDA-MB 231 cells (1×10^5 cells/well in 96-well plates) were treated with free MMC, MMC-GalG/g/PMMA, and MMC-GalG/g/PMMA@BIS nanogel, we employed an Annexin V-FITC/PI staining assay. This flow cytometry-based method enabled us to distinguish between early apoptotic, late apoptotic, and necrotic cell populations, providing a comprehensive picture of cell death mechanisms induced by our treatments.

2.2.5.6. ROS activity. Further, we investigated the generation of reactive oxygen species (ROS) in treated cells (free MMC, MMC-GalG/g/PMMA, and MMC-GalG/g/PMMA@BIS nanogel) using the DCFH-DA assay. MDA-MB 231 cells were inoculated at a density of 1×10^5 cells/well to initiate ROS measurement study. ROS production is often associated with cellular stress and can be a mechanism by which certain anticancer drugs exert their effects. By measuring DCF fluorescence intensity, we were able to compare the ROS-inducing potential of our nanogel formulations to that of free MMC.

2.2.5.7. Scratch wound healing assay. Lastly, to assess the impact of our formulations (free MMC, MMC-GalG/g/PMMA, and MMC-GalG/g/PMMA@BIS nanogel) on cell migration, a crucial aspect of cancer metastasis, we performed a scratch wound healing assay. We created a uniform wound across a monolayer of MDA-MB-231 cells (2×10^3 onto the 12-well plate) and monitored wound closure over time in the presence of our treatments. This assay provided insights into the potential anti-metastatic properties of our nanogel formulations.

2.2.5.8. Subcellular localization using Lysotracker Green. By labeling the cells with fluorescent probes specific to the organelle, the colocation of nanoparticles in subcellular organelles was visualized. The MDA-MB-231 cells were planted in confocal microscope dishes for attachment, and then incubated with rhodamine-loaded nanogel for 2, and 6 h. Rinsed with PBS, the cells were stained with LysoTracker™ Green DND-26 (Invitrogen, USA), according to the manufacturer's protocol. Subsequently, the cells were fixed with paraformaldehyde, stained using DAPI for nucleus, and eventually observed using CLSM.

2.2.5.9. Hemocompatibility study. In vitro hemocompatibility studies were conducted in accordance with ASTM F756–00 (2000) standards. Hemolytic indices were determined as per ISO 10993-4, with values below 2 % indicating non-hemolytic, 2.0–5.0 % slightly hemolytic, and above 5.0 % hemolytic behavior [36,39]. Blood samples from healthy mice were collected in sodium citrate tubes and processed in triplicate.

The hemolytic activity of formulations (MMC-GaLg/g/PMMA, and MMC-GaLg/g/PMMA@BIS nanogel) were assessed using a modified protocol based on established methods [36,39]. Briefly, red blood cells (RBCs) component isolated from freshly collected mouse blood were incubated with various concentrations (5–30 µg/mL) of the MMC-GaLg/g/PMMA@BIS nanogel and MMC-GaLg/g/PMMA formulations for 12 h at 37 °C. PBS and Triton X-100 served as negative and positive controls, respectively. Hemolysis was determined by measuring hemoglobin release (540 nm) into the supernatant following centrifugation, using the reported formula

$$\text{RBC Hemolysis (\%)} = \frac{(\text{Abs sample} - \text{Abs negative control})}{(\text{Abs positive control} - \text{Abs negative control})} \times 100 \quad (4)$$

To complement our quantitative hemolysis assay, we conducted microscopic examinations of erythrocyte morphology. This qualitative analysis provided visual evidence of any potential damage to red blood cell structure induced by our formulations. We prepared slides by adding a single drop of blood incubated with our MMC-GaLg/g/PMMA and MMC-GaLg/g/PMMA@BIS nanogel formulations, rinsed excess blood with pH 7.4 PBS, and examined the samples under a bright-field microscope at 40× magnification [49]. This morphological assessment offered valuable insights into the interaction between our nanogel formulations and erythrocyte membrane integrity. By observing any changes in cell shape, size, or integrity, we could corroborate our quantitative hemolysis data and gain a more comprehensive understanding of the hemocompatibility of our formulations.

2.2.6. In-vivo study

We conducted a comprehensive efficacy and safety study to evaluate the in vivo performance of our MMC-GaLg/g/PMMA, and MMC-GaLg/g/PMMA@BIS nanogel systems. All experimental procedures adhered to the established protocols. Our investigation focused on the In-vivo MMC release, biodistribution, tumor regression study, and survival analysis in a 4T1 xenograft murine breast cancer model (female BALB/c mice). Ethical approval for animal experiments was obtained from the CSIR-CDRI Animal Ethics Committee (IAEC/2023/77/Renew-0 / Sr. no.8).

2.2.6.1. Pharmacokinetics and biodistribution studies. For the In vivo MMC release and biodistribution study, we used female BALB/c mice (3–5 weeks old, 16–22 g) inoculated with 4T1 cells in the lower groin region of the mammary fat pad to induce tumors. We initiated the experiment when tumor volumes reached approximately 90–111 mm³ across all animals [7,50].

We divided the animals into three groups of five mice each. Group 1 received free MMC intravenously (IV), while Groups 2 and 3 were treated intratumorally (IT) with free MMC and MMC-GaLg/g/PMMA@BIS nanogel (10 % w/v), respectively. All treatments contained an MMC dose equivalent to 4 mg/kg. We collected blood samples

(200 µL) at predetermined time points (0.083, 0.25, 0.5, 1, 2, 4, 6, 8, 12, and 24 h) and analyzed MMC concentrations in plasma using validated LC-MS/MS (MMC/LC-MS/MS method in supplementary 2.2) and the data are represented as mean ± SD ($n = 5$). The plasma concentrations vs. time profiles were extracted by PK Plus™ 2.0 software using non-compartmental analysis.

To visualize the biodistribution of our nanogel, Evans blue loaded-GaLg/g/PMMA@BIS nanogel, and GaLg/g/PMMA were analyzed by a whole-body imaging system (Caliper IVIS Kinetic) to track its distribution qualitatively. We processed the images using Living Image® Software 4.4.

2.2.6.2. Survival analysis. The survival analysis offered a clinically relevant endpoint to assess the overall therapeutic benefit of our nanogel formulation compared to free MMC and other control treatments. Our survival analysis study expanded, utilizing a new cohort of animals divided into five groups of six each. We standardized initial tumor volumes between 90 and 111 mm³ across all subjects before administering treatments. The groups received varying interventions: Group 1 received an intratumoral injection of 60 µL PBS. Group 2, administered a single intravenous dose of 4 mg/kg free MMC solution. Groups 3, 4, and 5 received a single intratumoral injection of free MMC solution, MMC-GaLg/g/PMMA formulation, and MMC-GaLg/g/PMMA@BIS nanogel containing MMC equivalent to 4 mg/kg, respectively. We conducted this survival study over a 40-day period, carefully monitoring the survival rates of animals in each group. The resulting survival data underwent rigorous analysis using GraphPad Prism 7.04 software (GraphPad Software Inc.), providing us with valuable insights into the long-term efficacy of our nanogel formulation compared to conventional treatments.

2.2.6.3. 4T1-breast tumor xenograft BALB/c model and tumor regression study. In our comprehensive in vivo study, we sought to evaluate the efficacy of our MMC-GaLg/g/PMMA@BIS nanogel system in a clinically relevant model of triple-negative breast cancer. We utilized young female BALB/c mice, weighing 18–20 g, to establish an orthotopic tumor model that closely mimics human disease progression. Our experiment began with the implantation of 4T1 cells (5×10^5 cells per animal) into the mammary fat pad near the left lower abdominal quadrant of each mouse, strategically chosen to simulate the primary site of breast cancer development [6,45]. We closely monitored tumor growth until volumes reached 100–110 mm³, ensuring a consistent baseline for our therapeutic interventions. The selection of female BALB/c mice was based on their established higher susceptibility to the specific tumor model employed, as documented in previous literature [51].

Upon achieving the desired tumor volume, we randomly divided the mice into four groups of five animals each, minimizing bias and ensuring statistical validity. The treatment groups received single intratumoral injections of saline (control), free MMC, or MMC-GaLg/g/PMMA@BIS nanogel, containing MMC equivalent to 4 mg/kg in a 100 µL volume. We utilized a syringe fitted with a 21-gauge, 1-in. needle for precise intratumoral administration, ensuring consistent delivery across all groups.

Following treatment, we implemented a rigorous monitoring schedule to track tumor progression. We measured the combined length and width (T + L) of each group's tumor at the start of treatment and on the 21st day of the study. Throughout this period, we accurately recorded tumor volumes, and body weights, providing a comprehensive view of both treatment efficacy and potential systemic toxicity. Tumor volumes were calculated by the established formula Volume (mm³) = (Length × width²) / 2, where length and width parameters are taken in mm.

At the study's conclusion on day 21, we humanely euthanized the animals and carefully harvested the tumors for further analysis. Tumors were immediately weighed, to provide a direct measure of treatment impact on tumor burden, and tissues were preserved in formalin for

subsequent histological examination. Our histological analysis involved embedding tissues in paraffin, sectioning at 4–8 µm thickness, and staining with hematoxylin and eosin (H&E) for microscopic evaluation of cellular architecture and morphology.

2.2.6.4. Ex-vivo assessment of tumor cell proliferation and apoptosis. Ki-67 and TUNEL are two valuable immunohistochemical markers used to assess tumor proliferation and apoptosis, respectively. The combined use of Ki-67 (Invitrogen, USA) TUNEL (DeadEnd™ Fluorometric TUNEL System, Promega) assays, along with advanced imaging techniques like confocal microscopy, provides a valuable tool for assessing tumor biology and evaluating the efficacy of therapeutic interventions. (Methodology in supplementary Sections 2.4 and 2.5).

This multifaceted study design allowed us to assess the various aspects of our MMC-GalG/g/PMMA@BIS nanogel system's performance, including antitumor efficacy, safety profile, and histological impact on tumor tissue architecture. By combining these diverse endpoints, we aimed to build a robust body of supporting evidence for the potential of our nanogel-based drug delivery system in the treatment of breast (TNBC) cancer. The data generated from this study will not only inform further optimizations of our formulation, but also provide crucial insights for the design of future preclinical and potential clinical investigations.

2.2.7. Statistical analysis

Rigorous statistical analysis was employed to ensure the reliability of findings. Multiple experiments (minimum of three) were conducted, and data were analyzed using one-way ANOVA to compare groups while minimizing the risk of errors. Statistical significance was determined using a *p*-value threshold of 0.05 or 0.001. GraphPad Prism 7.04 (GraphPad Software, Inc.) was used for data analysis.

3. Results and discussion

3.1. Preparation of Redox Responsive Cross-linked Gellan Gum Nanogel (GalG/g/PMMA@BIS nanogel)

The redox-responsive nanogel was synthesized through free radical polymerization, followed by cross-linking using a microwave-assisted approach, as detailed in the methodology Section 2.2.1. RSM was implicated in the experiments to establish and optimize the relationships between the test factors. In this research, the amount of GalG (A), amount of MMA/N, N BIS Cyst (B), and amount of APS (C) were selected as parameters affecting the dependent variables. Design-Expert® statistical software (Trial version 11.1.2.0, 64-bit, Stat Ease, Inc., Minneapolis) was used to examine the effect of parameters on response performance.

A total of fourteen independent experiments comprising two central points, were assigned by software utilizing Box-Behnken optimization design (BBD-RSM). (Table S1). All experiments were conducted randomly, and the inputs of independent variables were selected according to preliminary data. Each independent factor was associated with two distinct coded hierarchies (-1, 1) (Table 1). The general quadratic polynomial model (second order) with three independent factors (A, B, and C) is represented by bellow equation, [52]

$$Y = \beta_0 + \beta_1 A + \beta_2 B + \beta_3 C + \beta_{11} A^2 + \beta_{22} B^2 + \beta_{33} C^2 + \beta_{12} AB + \beta_{13} AC + \beta_{23} BC + \epsilon \quad (5)$$

Where: Y represents the predicted response, β_0 is the axis-intercept, β_1 - β_3 are linear coefficients for variables A-C, β_{11} - β_{33} are quadratic coefficients for A-C, β_{12} - β_{23} represent interaction effects, and ϵ is the error term.

3.2. Influence of operational parameters on responses

Following the preparation of the redox-responsive cross-linked GalG/g/PMMA@BIS nanogel, a comprehensive statistical analysis was conducted to evaluate the factors affecting key response variables, including %GE, PS, PDI, ZP, and %EE, providing deeper insights into the formulation's optimization. Table 2, shows the ANOVA results for BBD-RSM models generated by the software. The *p*-values lower than 0.05 confirm that the overall model and model terms are significant. Terms A, B, and C were found to be significant (*p* < 0.05) for models generated for response variables %GE, ZP, and %EE. This indicates that these terms have a statistically relevant effect on the responses. Interestingly, term A was non-significant for factors like PS and PDI, suggesting that its influence was not critical for these specific responses. Furthermore, the quadratic terms A^2 , and C^2 and the interaction coefficient AC and BC were found to be significant (*p* < 0.05) for % GE, and PS, while A^2 , C^2 , and B^2 are significant for ZP, and % EE. The quadratic terms (A^2 , B^2 , and C^2) allowed us to explore how changes in the levels of factors A, B, and C affect the responses (%GE, PS, PDI, ZP, and %EE) not only linearly but also quadratically. The high R^2 values (0.995, 0.990, 0.990, 0.998, and 0.994 for % GE, PS, PDI, ZP, and EP, respectively) indicate that the model generated from the design expert is good fit for the data, suggesting that the chosen factors effectively explain a large proportion of the variation in the response variables. Additionally, the non-significant lack-of-fit values (*p* > 0.05, % GE: 0.615; PS: 0.427; PDI: 0.371; ZP: 0.429, and EE: 0.411) further strengthen the model's validity, implying that the chosen model adequately explains the relationship between the factors and the response variables. Furthermore, adjusted R^2 values and predicted R^2 values were in close agreement with each other (difference < 0.2), demonstrating that the generated mathematical model was able to predict accurately the selected responses based on the various input variables.

Additionally, the accuracy of the statistical regression model was decided by unraveling the diagnostic plot of predicted vs. actual response values. The predicted and actual responses are visualized in Fig. 1 [B], confirms that the predicted and actual response values exhibit a close correspondence, indicating a good fit without any significant deviations from the line of fit (Table S2). The 2D [Fig. 1 A] and 3D [Fig. S1 A] response surface plots showed the impact of different process variables (A, B, and C) on response variable values (%GE, PS, PDI, ZP, and %EE). These plots identify the optimal preparation conditions for nanogel, potential interactions between variables, and the overall relationship between the variables (A, B, and C) and the responses (%GE, PS, PDI, ZP, and %EE). The coded equations representing the relationships between the independent variables and responses were extracted from the model and presented as Eqs. (6) to (10). Significant positive constraint was observed for factor B (amount of MMA/N, N BIS Cyst), and factor C (amount of APS) (Eq. (6)), enhancing grafting efficiency. These findings align well with prior research suggesting that a higher amount of polymer, monomer, or initiator/cross-linker contribute to enhancing grafting efficiency [53,54]. Interestingly, Eqs. (7) and (8) revealed a negative correlation between factors B and C and particle size and PDI, indicating that increasing these factors led to larger particles. This outcome contradicts our goal of reducing particle size and PDI (Table 1). One possible explanation behind this observation is that higher concentrations of monomers increase the availability of monomer molecules for polymerization reactions, leading to the formation of larger nanogel particles. Additionally, the elevated levels of free radicals and cross-linkers associated with increased monomer concentrations could accelerate the polymerization process, further contributing to particle growth [55,56]. Eq. (10) revealed a positive correlation between polymer, monomer, and free radical concentrations and %EE, corroborating our initial hypothesis (Table 1). To achieve optimal %EE, a careful balance of these factors must be maintained.

Higher monomer and free radical concentrations had a negative impact on PDI, ZP, and %EE.

Table 2
ANOVA Table for Box-Behnken Design (BBD-RSM).

Source	% GE		PS		PDI		ZP		% EE		
		Pvalue		Pvalue		Pvalue		Pvalue		Pvalue	
Model		0.0001		< 0.0001		< 0.0001		0.0001		0.0001	Significant
A		0.0010		–		–		0.0001		0.0003	
B		0.0001		< 0.0001		< 0.0001		0.0001		0.0001	
C		0.0001		< 0.0001		< 0.0001		0.0001		0.0001	
AC		0.0016		0.0001		< 0.0001		0.0258		0.0149	
BC		0.0001		0.0254		< 0.0001		–		0.0001	
A^2		0.0002		0.0021		–		0.0095		0.0011	
B^2		–		–		–		0.0001		0.0010	
C^2		0.0001		0.0108		–		0.0001		0.0033	
Lack of significance		0.6149		0.4271		0.3708		0.4289		0.4110	Not significant

Note: * A-Amount of GalG, B-Amount of MMA/N, N Bis acryloyl cystamine, and C-Amount of APS, A^2 , B^2 , and C^2 represent the quadratic terms.

$$\begin{aligned} \%GE = 94.12 &+ (-) 0.625 \times A + 2.3 \times B + 1.925 \times C + 0.8 \times AC \\ &+ 1.4 \times BC + 1.32 \times A^2 + (-) 2.03 \times C^2 \end{aligned} \quad (6)$$

$$\begin{aligned} PS = 120.23 &+ (-) 16.3375 \times B + (-) 10.5375 \times C + (-) 10.675 \\ &\times AC + 4 \times BC + 7.355 \times A^2 + 5.33 \times C^2 \end{aligned} \quad (7)$$

$$\begin{aligned} PDI = 0.196857 &+ (-) 0.02125 \times B + (-) 0.04125 \times C + (-) 0.0225 \times AC + (-) 0.03 \times BC \end{aligned} \quad (8)$$

$$\begin{aligned} ZP = -28.1 &+ (-) 1.1625 \times A + (-) 1.5 \times B + (-) 3.0875 \times C + (-) 0.325 \times AC + 0.4625 \times A^2 + 2.1375 \times B^2 + (-) 1.5375 \times C^2 \end{aligned} \quad (9)$$

$$\begin{aligned} \%EE = 93.725 &+ 0.79375 \times A + 1.30375 \times B + 1.5425 \times C + 0.47 \\ &\times AB + 1.5425 \times BC + (-) 0.98 \times A^2 + (-) 0.985 \times B^2 \\ &+ 0.7575 \times C^2 \end{aligned} \quad (10)$$

3.3. Numerical optimization and validation

The numerical optimization approach was applied to identify the optimal condition for responses (i, e; %GE, PS, ZP, and %EE). The values of different variables in the numerical optimization process were adjusted as per our goal, aiming to maximize the %GE, and ZP, while minimizing the PS, and PDI. The desirability function method was employed to obtain the best responses [Fig. S1 (B)]. Based on the high desirability score (global desirability score; 0.98), a new experiment was performed to validate the model. The optimal conditions of factors A, B, and C included an amount of 200 mg of A, 323.25 mg of B, and 15 mg of C. Under these conditions, the % GE, PS, PDI, ZP, and %EE were 97.1 %, 123.30 nm, 0.15, -22.2 mV, and 94.2 % with percent bias of 1.12, 0.32, 15.00, 27.21, and 1.36 %, respectively. (Table 3).

3.4. Drug loading efficiency

To optimize drug loading and ensure nanogel stability, we systematically evaluated three different nanogel/MMC ratios: 4:1, 2:1, and 1:1. Our results indicated in Table S3 that a 2:1 ratio yielded the most optimal balance between drug loading efficiency and nanogel stability.

Higher drug loading ratios (4:1) led to increased internal stress within the nanogel network, potentially compromising its structural integrity. Lower ratios (1:1) resulted in lower drug encapsulation efficiency, reducing the therapeutic efficacy. The 2:1 ratio provided a suitable compromise, ensuring both effective drug delivery and nanogel stability [57]. By carefully optimizing the drug loading ratio, we have developed a stable and effective nanogel formulation that can deliver therapeutic agents to target sites.

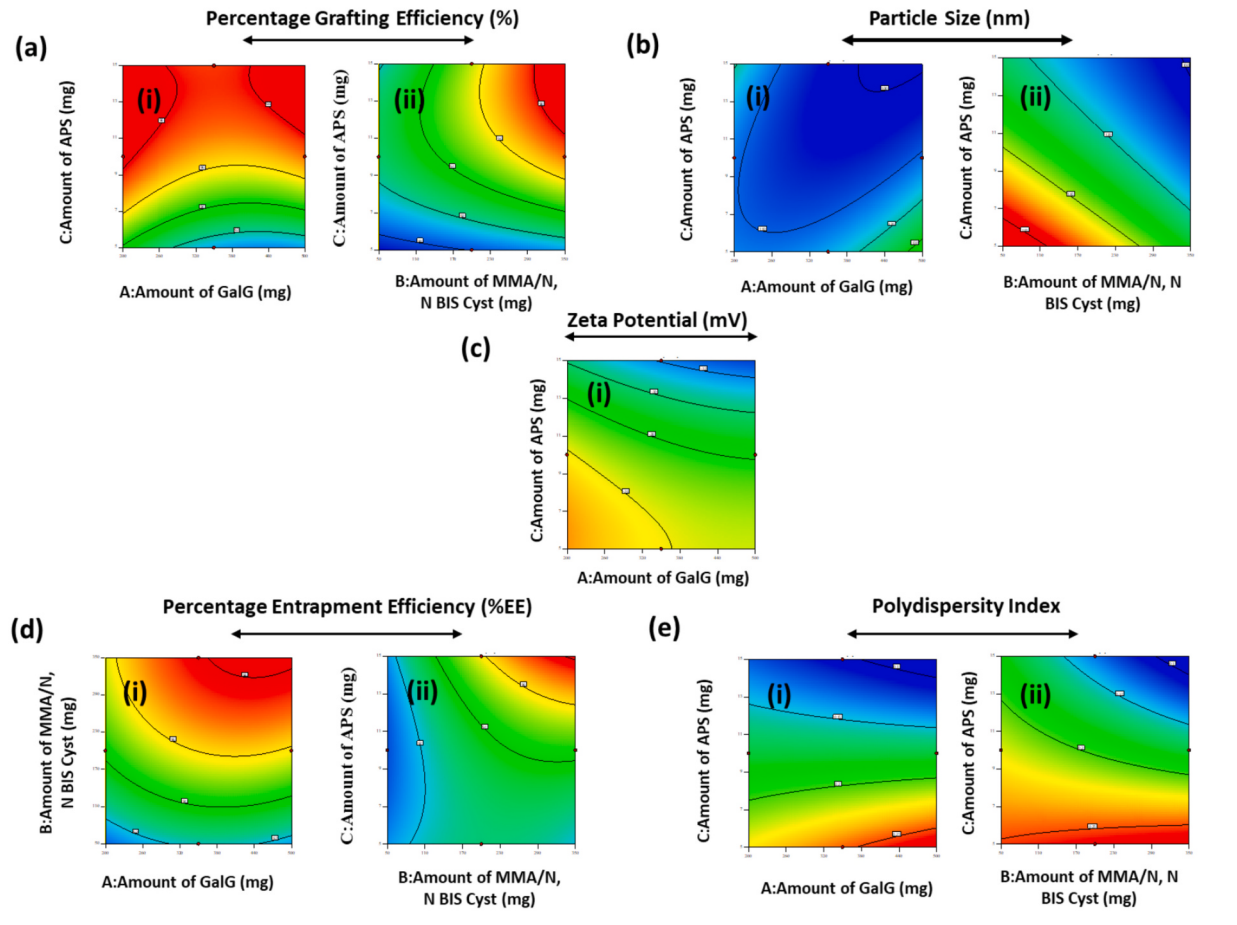
3.5. Physicochemical and morphological characterization of cross-linked nanogel

A comprehensive physicochemical characterization focusing on particle size, PDI, zeta potential, morphological characterization, and rheological behavior was performed to assess the potential of developed nanogel carriers in breast cancer treatment. MMC-GalG/g/PMMA@BIS nanogels were fabricated by free radical polymerization technique followed by cross-linking with a redox-sensitive cross-linker. A control batch without a cross-linker was also prepared to observe the effect of disulfide cross-linking on the stability as well as the in-vitro efficacy of nanogels. The quality control parameters of the MMC-GalG/g/PMMA@BIS nanogel such as particle size, grafting efficiency, surface zeta potential, and size distributions etc. are represented in Table S2. Following the experiments conducted with the 14 formulations listed in Table S1, the average size of the nanogel was found to range from 100 to 200 nm, as detailed in Table S2. After optimization through RSM, the optimized batch was prepared, and Table 4 shows that the mean particle size of the optimized MMC-GalG/g/PMMA@BIS nanogel was 123.37 ± 0.98 nm along with a PDI of 0.15 ± 0.01 indicating a monodisperse population [Fig. 2F (a)]. As anticipated, coded Eq. (7) revealed an inverse correlation between cross-linker or monomer concentrations and particle size, consistent with prior studies. This observation is attributed to the formation of a denser nanogel network at higher cross-linker levels [56,58]. A narrow PDI indicates a homogeneous particle size distribution, enhancing the potential of MMC-GalG/g/PMMA@BIS nanogels for drug loading and delivery applications. The recorded zeta potential values of -23 to -35 mV advise good colloidal stability of the nanogel particles, effectively preventing the aggregation and thus enhancing the stability of the formulation. The particle size and stability are crucial for effective intratumoral delivery, as they allow the nanogel particles to penetrate the complex tumor microenvironment without premature aggregation.

DLS analysis [Fig. S2 (a), (b); Table S6] for redox susceptibility evaluation demonstrated a significant increase in MMC-GalG/g/PMMA@BIS nanogel size upon DTT titration, ranging from 138 nm to 590 nm, upon DTT titration for 24 h, suggesting partial disassembly of the nanostructure due to disulfide bond dissociation under reducing conditions (10 mM DTT). The difference in size between the MMC-GalG/g/PMMA@BIS nanogel (123 nm) and MMC-GalG/g/PMMA (319 nm) depicted in Table 4 is due to crosslinking, which introduces covalent bonds that reduce polymer chain mobility, resulting in a more compact, stable structure and limiting expansion in aqueous solutions. In contrast, MMC-GalG/g/PMMA polymer chains are free to interact with the solvent, yielding a larger hydrodynamic size. This observation was corroborated by TEM [Fig. 4A (a), and (b)], which revealed a morphological transition from spherical particles to deformed structures in the reductive environment. These findings contribute to the advancement of redox-responsive nanogels for intratumoral MMC delivery in breast cancer treatment, highlighting the potential of this nanocarrier system

[A]

2D Response Surface Plot (Box-Behnken Design)



[B]

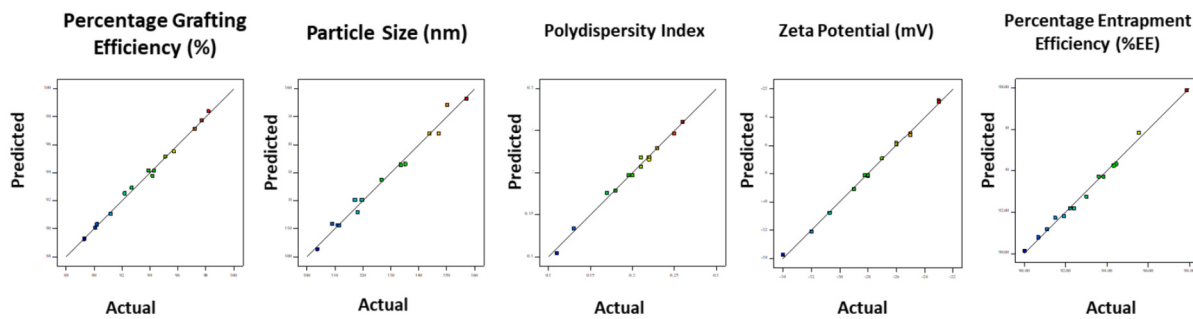


Fig. 1. Response surface [A], and Predicted Vs. actual [B] plot: [A] 2D illustrations depicting the effect of independent process variables on dependent variables (a-e), [B] Predicted Vs. Actual plot for responses like %GE, PS, PDI, ZP, %EE.

Table 3

Validation of GalG/g/PMMA@BIS nanogel parameters through Box-Behnken design (RSM-BBD).

Variables	%GE		PS		PDI		ZP		%EE			
	A	B	C	Prd.	Atl.	Prd.	Atl.	Prd.	Atl.	Prd.	Atl.	
200	323	15	98.2	97.1	122.9	123.3	0.13	0.15	-30.5	-22.2	95.5	94.2

Note: A, B, and C are the amount of GalG, MMA/N, N BIS Cyst, and APS, respectively, and Prd: Predicted, Atl: Actual.

for targeted therapy.

SEM analysis [Fig. 2A (a), (b)] revealed a distinct internal-morphological transformation from the GalG to the GalG/g/

PMMA@BIS nanogel, characterized by a porous and intercalated structure resulting from PMMA chain insertion and covalent cross-linking due to BIS. SEM results corroborated the previous findings on

Table 4

Characterization of MMC-loaded formulation.

MMC loaded formulation	PS (nm)	PDI (–)	ZP (mV)	DL. (%w/w)
MMC-GalG/g/PMMA	318.8 ± 2.61	0.24 ± 0.02	-18.85 ± 0.78	32.45 ± 0.66
MMC-GalG/g/PMMA@BIS	123.37 ± 0.98	0.15 ± 0.01	-22.17 ± 0.31	45.54 ± 0.42

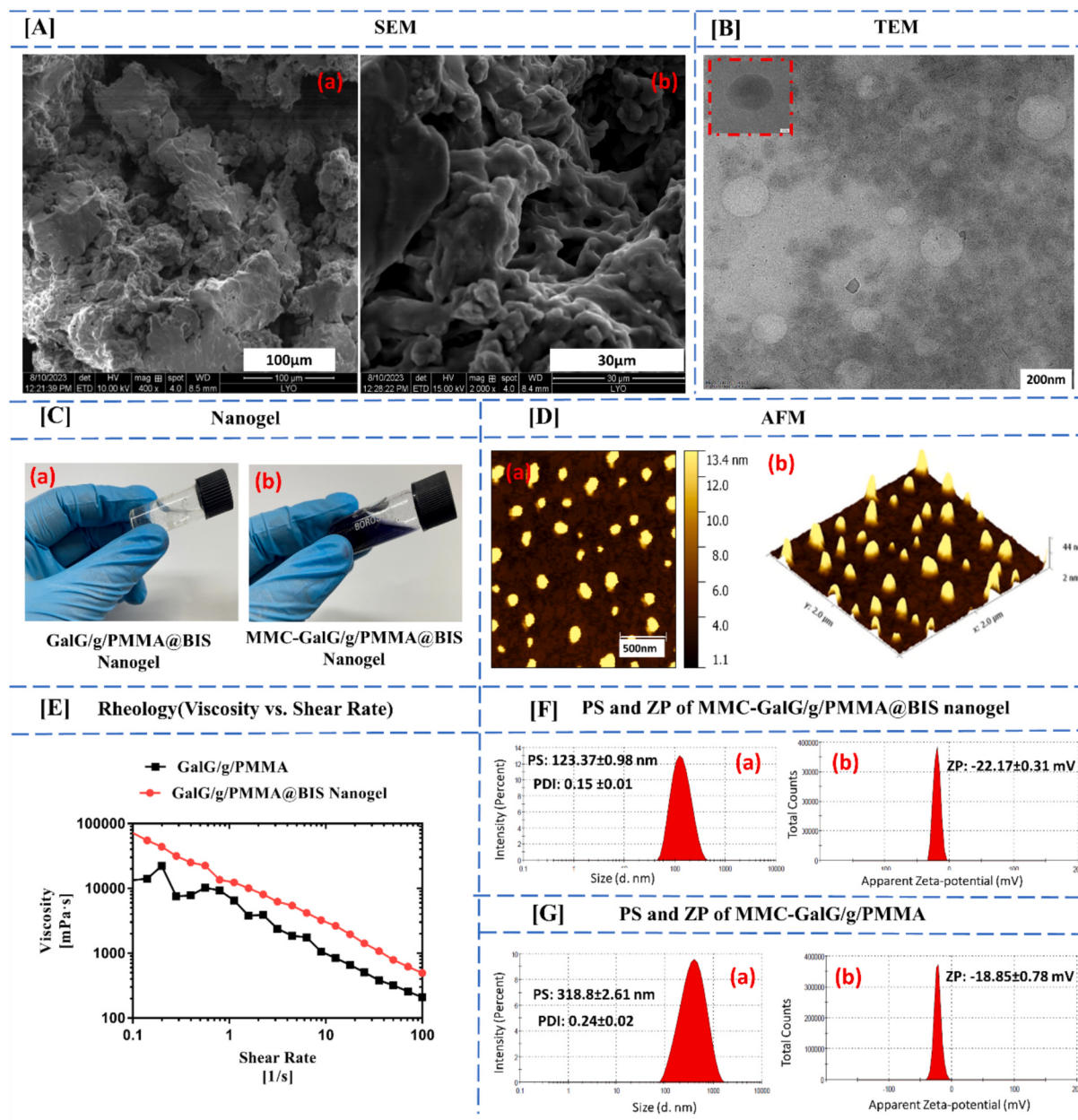
Note: $n = 3$; Mean ± SD, PDI-Polydispersity index.

Fig. 2. [A] SEM evaluation of MMC-GalG/g/PMMA@BIS nanogel before (a) and after cross-linking (b). The images highlight the morphological changes that occur during the cross-linking process, including the development of a porous and intercalated structure after cross-linking. [B] TEM evaluation revealing a spherical morphology of MMC-GalG/g/PMMA@BIS nanogel (Scale bar 200 nm). [C] Blank and MMC loaded formulations, (MMC-GalG/g/PMMA@BIS nanogel), [D] AFM evaluation of MMC-GalG/g/PMMA@BIS nanogel: (a, b) Two-dimensional (2D) and three-dimensional (3D) Images (Scale bar 500 nm), [E] Shear viscosity vs. shear rate plot for MMC-GalG/g/PMMA@BIS nanogel, and MMC-GalG/g/PMMA. [F] (a, b) Particle size, and zeta potential of MMC-GalG/g/PMMA@BIS nanogel, [G] (a, b) Particle size and zeta potential of MMC-GalG/g/PMMA.

the morphological characteristics of other nanogel systems [36,59,60]. AFM imaging [Fig. 2D (a), and (b)] revealed a spherical morphology of the nanogel particles, a desirable characteristic for intratumoral injection applications due to its potential for smooth needle passage and

reduced blockage risk. The high-resolution morphological insights by TEM [Fig. 2 B], corroborate the findings obtained from AFM and DLS studies. The smaller particle size observed by TEM compared to DLS is attributed to the measurement of dehydrated particles by TEM, while

DLS determines the hydrodynamic diameter [61].

Syringeability is a crucial factor for the successful delivery of nanogel at the injection site. It ensures smooth injection, minimizes patient discomfort, and prevents needle clogging. Evaluating nanogel's rheological behavior, focusing on its shear-thinning behavior is crucial for assessing injectability [48,62]. The rheological study of GalG/g/PMMA, and GalG/g/PMMA@BIS nanogel was performed at a concentration of 0.5%w/w. The semi-log plot [Fig. 2 E] of shear viscosity (mPa·s) vs shear rate (0.1 to 100 Sec⁻¹) reveals that the viscosity decreases with an increase rate of shear, which confirms the shear thinning or non-

Newtonian behavior of the nanogel system. This non-Newtonian behavior arises from the alignment of cross-linked polysaccharide chains in response to applied stress, alignment reduces the viscosity of nanogel [63]. These findings collectively support the suitability of the developed nanogel system for injection and provide valuable insights into its structural and rheological properties, which are essential for its potential application in breast cancer treatment through intratumoral drug delivery.

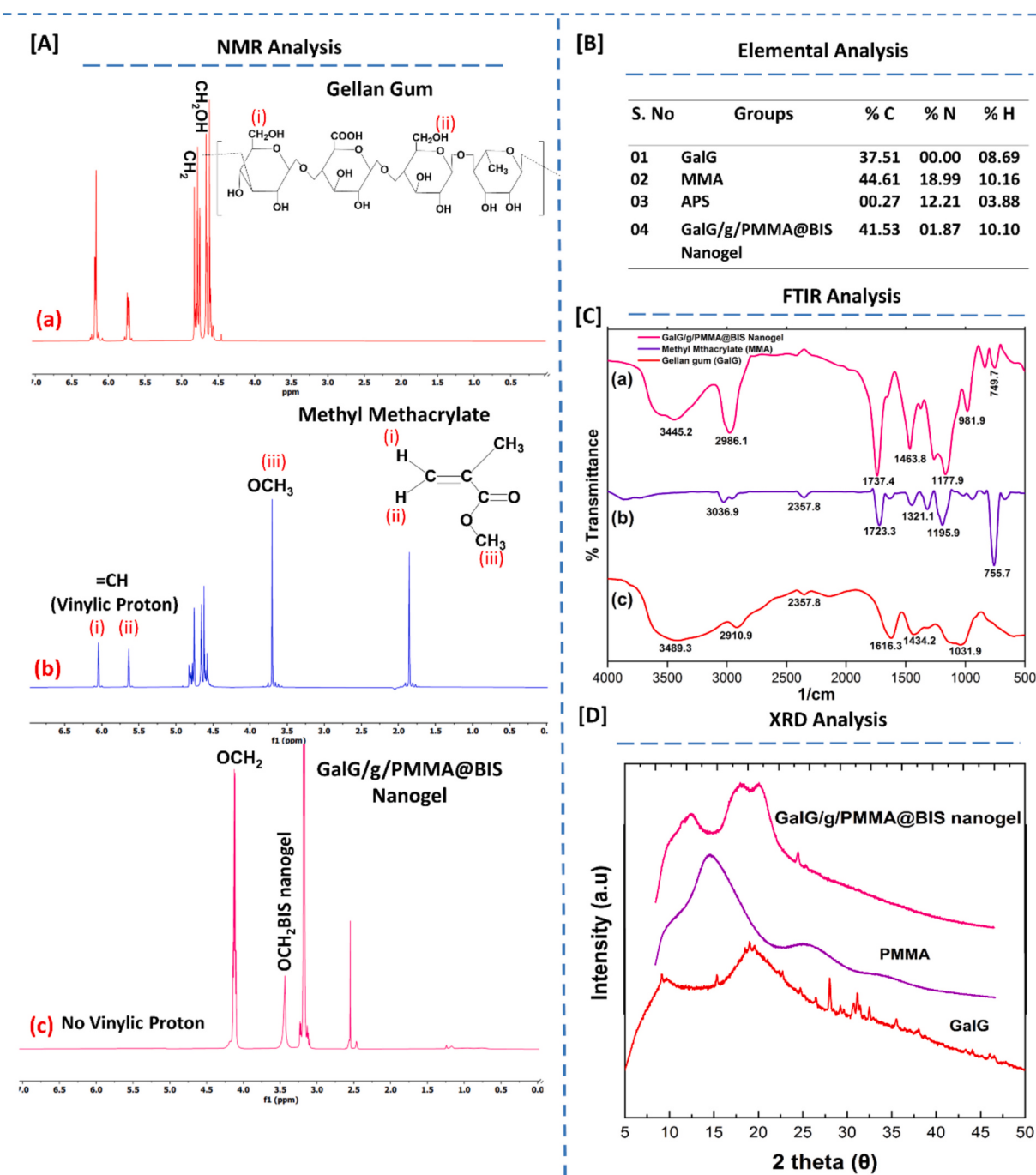


Fig. 3. Proton NMR (¹H) spectrum for structural elucidation of [A]: (a) gellan gum (GalG), (b) methyl methacrylate (MMA), and (c) product (GalG/g/PMMA@BIS Nanogel). [B]. Elemental composition of gellan gum (GalG), methyl methacrylate (MMA), and product (GalG/g/PMMA@BIS Nanogel). (C) FTIR spectrum of gellan gum (GalG), methyl methacrylate (MMA), and product (GalG/g/PMMA@BIS Nanogel) respectively. (D) XRD spectra of GalG, PMMA, and GalG/PMMA@BIS nanogel.

3.6. Evaluation of cross-linking

3.6.1. FTIR spectroscopy

Fourier Transform Infrared (FTIR) spectroscopy study was implemented to compare the chemical functionalities of gellan gum (GalG), monomer (MMA), and the synthesized GalG/g/PMMA@BIS nanogel. The spectra, depicted in Fig. 3C, divulge characteristic peaks corresponding to the chemical functionality within each material. Both the, GalG and GalG/g/PMMA@BIS nanogel share some characteristic peaks associated with their functional groups. The band at 2910.9, and 2357.8 cm^{-1} is ascribed to the stretching vibrations of -CH, and -CH₂ groups respectively. The broad peaks at 3489.3 cm^{-1} correspond to the O—H stretching vibration in GalG [64,65]. Interestingly, this peak in the GalG/g/PMMA@BIS nanogel shows a slight shift and becomes shorter. This might be due to a potential participation during the reaction. Peaks at 1031.9, and 1616.3 cm^{-1} are assigned to C=O, and C=O stretching vibrations respectively, while the peak at 1434.2 cm^{-1} corresponds to the O—H bending vibration [64]. In the MMA spectrum, distinct peaks were observed at 2357.8 cm^{-1} corresponding to -CH stretching and at 1195.9 cm^{-1} attributed to C-O-C stretching. The disappearance of the vinylic C=C stretching vibration peak at 1723.3 cm^{-1} in the final nanogel spectrum indicates its involvement in the grafting reaction [65]. Successful grafting and cross-linking were further confirmed in the nanogel spectrum by the appearance of an additional peak at 1737.4 cm^{-1} , signifying methacrylation of the gellan gum [66]. Additionally, the absorption peak at 1463.8 cm^{-1} , assigned to the -NH in-plane bending vibration of the BIS amide group, supports the formation of the cross-linked nanogel structure.

3.6.2. NMR spectroscopy

The structural analysis of GalG, MMA, and the resulting GalG/g/PMMA@BIS nanogel were performed using ¹H NMR spectroscopy. For gellan gum, peaks in the 6.17–6.19 ppm range were assigned to hydroxyl (-OH) groups attached to the ring, while the peak at 4.83 ppm represented primary hydroxyl protons. The peak at 4.57 ppm indicates the presence of the -CH- group in the glucose unit. The -CH₂- protons were identified by a peak at 4.66 ppm, confirming the typical structure of gellan gum [Fig. 3A, (a)] [67,68]. In the case of MMA (methyl methacrylate), vinylic protons were observed between 5 and 6 ppm, indicating the presence of the vinyl group. The methoxy (-OCH₃) group was detected at 3.77 ppm, and methyl (-CH₃) protons appeared in the 1–2 ppm range, aligning with MMA's expected structure [Fig. 3A, (b)] [67]. Interestingly, the final product lacked one of the MMA's vinylic proton signals, suggesting its potential involvement in the reaction. For the synthesized nanogel, distinct peaks provided evidence of successful chemical modification through the reaction of gellan gum with BIS acrylamide via free radical addition. Peaks at 3.56 and 3.81 ppm were attributed to R-OH₂ groups, while the prominent peak at 3.65 ppm corresponded to R-O-CH₂ groups formed by crosslinking gellan gum's primary hydroxyl groups with BIS [Fig. 3A, (c)]. These results confirm the structural changes and successful formation of the nanogel [69].

3.6.3. Elemental (C, N, H) analysis

The elemental composition results for gellan gum (GalG) and the GalG/g/PMMA@BIS nanogel, presented in Fig. 3 B, provided further evidence of the successful synthesis and modification of the nanogel system. The analysis revealed a significant increment of carbon and nitrogen percentage in the GalG/g/PMMA@BIS nanogel compared to the native GalG. This observation confirms the successful grafting and cross-linking of the poly (methyl methacrylate) (PMMA) chains onto the GalG backbone [69]. The increased carbon content is due to the presence of carbon-rich PMMA chains, while the presence of nitrogen likely results from the incorporation of the cross-linker (BIS, presumably N, N'-Bis (acryloyl)cystamine) into the nanogel structure. These elemental composition changes corroborate the findings from other characterization techniques, such as FTIR and NMR, and provide quantitative

evidence of the chemical modifications that occurred during nanogel synthesis.

3.6.4. X-ray diffractometer analysis

XRD analysis was performed to investigate the structural changes induced by grafting and crosslinking. The native GalG exhibited a semi-crystalline nature, as evidenced by the characteristic peaks at 15.25°, 27.94°, 31.25°, and 35.55° (20). In contrast, PMMA displayed an amorphous structure, characterized by a broad peak at 13.85° (20). The XRD pattern of the GalG/g/PMMA@BIS nanogel showed a reduction in the intensity of the characteristic GalG peaks and a broadening of the peak at 28.15° (20), indicating a decrease in crystallinity due to the incorporation of amorphous PMMA chains and the formation of a cross-linked network (Fig. 3D). These findings are consistent with previous studies on similar nanogel systems [44,70].

3.7. In vitro MMC-release and nanogel stability

In our comprehensive investigation of the MMC-GalG/g/PMMA@BIS nanogel system, we conducted a series of experiments to elucidate its drug release behavior and stability characteristics. These studies aimed to simulate the tumor microenvironment and assess the system's potential as a controlled drug delivery platform for mitomycin C (MMC). Having established the redox sensitivity and morphological characteristics of our nanogel system through previous studies, including TEM analysis, we proceeded to evaluate the in vitro drug release profile under reductive conditions.

The in vitro release of MMC from MMC-GalG/g/PMMA, and MMC-GalG/g/PMMA@BIS nanogel were examined under various conditions, including the presence of plasma (25 % in 10mMDTT), and a reducing environment (10 mM dithiothreitol, DTT) in PBS (5.5). Our findings, illustrated in Fig. 4 C, revealed several intriguing aspects of the nanogel's release kinetics.

Notably, plasma significantly accelerated MMC release from both the formulations. This observation further supported by previously published research, suggesting that the high affinity of the drug with plasma protein promotes its release [28]. Furthermore, the reducing environment created by DTT markedly influenced the release profile of MMC-GalG/g/PMMA@BIS nanogel compared to MMC-GalG/g/PMMA. In the simulated redox media (10 mM DTT), we observed a substantial increase in drug release from MMC-GalG/g/PMMA@BIS nanogel compared to MMC-GalG/g/PMMA. Specifically, the cumulative release at 72 h reached >70 % with DTT, contrasting sharply with only 24 % release in MMC-GalG/g/PMMA. This striking difference can be attributed to the reductive break-down of disulfide bonds within the MMC-GalG/g/PMMA@BIS nanogel structure, leading to its partial breakdown and subsequent drug liberation, which is absent in MMC-GalG/g/PMMA.

To further investigate the influence of the reducing agent on the release behavior of redox responsive MMC-GalG/g/PMMA@BIS nanogel, drug release study was also conducted in media devoid of DTT. As depicted in Fig. 4C, the nanogels exhibited significantly reduced MMC release in the absence of DTT, with only 13 % of the drug being released. In contrast, the presence of DTT led to a substantial increase in drug release, with over 70 % and 80 % release was observed in PBS and 25 % plasma, respectively. These results underscore the critical role of DTT in triggering the degradation of the disulfide bonds within the nanogel and facilitating the controlled release of the loaded drug.

To assess the long-term stability of our formulation, we conducted storage studies at temperature 4 °C and 25 °C in PBS (pH 5.5) over 8 weeks. The results, presented in Fig. 4B (a, b) and Table S4, demonstrate remarkable stability in context of particle size, distribution (PDI), and entrapment-efficiency (EE).

In addition to the storage stability studies, the stability of the MMC-GalG/g/PMMA@BIS nanogel was further evaluated under various physiological conditions, including 0.25 % NaCl and 10 % FBS. The 0.25

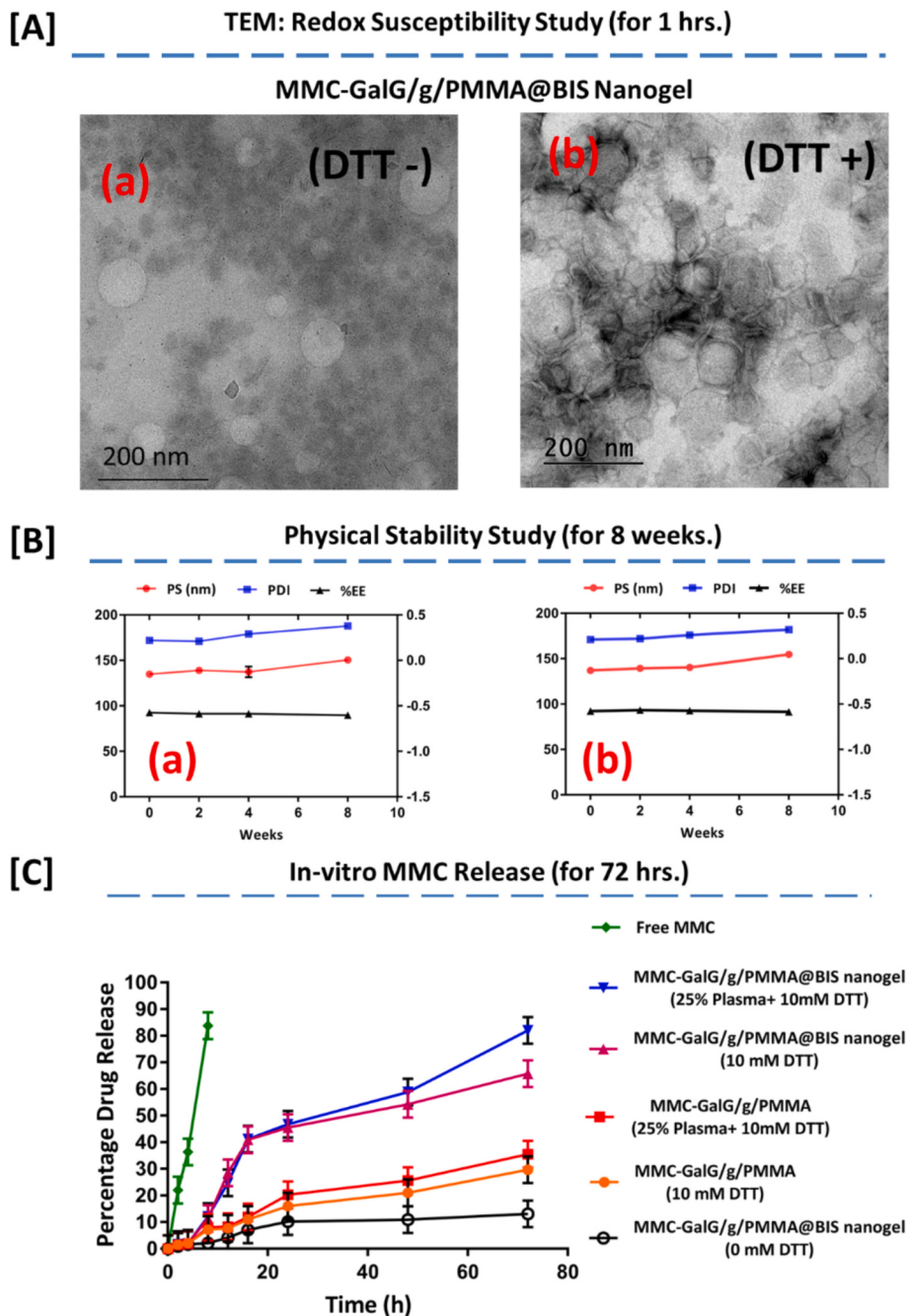


Fig. 4. [A] TEM images of redox susceptibility study of MMC-GalG/g/PMMA@BIS nanogel after 1 h in the absence (a), and presence (b) of the reductive environment (DTT) (Scale bar 200 nm), [B] long-term physical stability study of MMC-GalG/g/PMMA@BIS nanogel at 4 (a), and 25 °C (b), and [C] The release profiles of MMC from MMC-GalG/g/PMMA was assessed in PBS (orange line) and 25 % plasma containing 10 mM DTT (red line). Similarly, the release profiles of the MMC-GalG/g/PMMA@BIS nanogel was evaluated in PBS (magenta line) and 25 % plasma containing 10 mM DTT (blue line). These studies were conducted to understand the influence of DTT and simulated plasma conditions on the release behavior of the nanogels. Additionally, the release behavior of MMC-GalG/g/PMMA@BIS nanogel in media without DTT was studied (black line graph), revealing minimal release (13 %) compared to 65 % in the presence of DTT, underscoring the critical role of DTT in triggering drug release. Free MMC solution (green line) was used as a control to compare the release kinetics. Error bars represent standard deviation from triplicate measurements. (For interpretation of the references to colour in this figure legend, the reader is referred to the web version of this article.)

% NaCl solution mimics low ionic strength environments like interstitial fluid, helping to evaluate nanogel stability and interactions in ion-rich conditions. Meanwhile, the 10 % FBS simulates the biological milieu, particularly the interaction of nanogel with plasma proteins, offering insights into their behavior in the biological system. Throughout the study, no significant aggregation or changes in key parameters (Table S5) were observed, further confirming the robustness and stability of the nanogel system under both storage and physiological

conditions.

These findings collectively highlight the potential of the MMC-GalG/g/PMMA@BIS nanogel as a promising platform for controlled and intratumorally targeted delivery vehicle in cancer therapy. The system's ability to respond to tumor-specific stimuli, such as reducing environments, while maintaining stability under physiological conditions, presents exciting opportunities for enhancing the efficacy and safety of MMC-based treatments.

3.8. In vitro cellular studies

3.8.1. Cell cytotoxicity and proliferation assay

Our investigation into the cytotoxic efficacy of the MMC-GalG/g/PMMA@BIS nanogel system yielded compelling results, particularly when compared to free mitomycin C (MMC) and the non-crosslinked MMC-GalG/g/PMMA formulation. The MTT assay was conducted to evaluate the cytotoxic effects of the nanogel formulation on both MDA-MB-231 (cancerous) and HEK-293 (non-cancerous) cell lines, assessing the selectivity of the nanogel. The dose-response curves, illustrated in Fig. 5B, reveal a marked difference in the cytotoxic potency of these three treatments. Interestingly, while free MMC demonstrated cytotoxic effect, its efficacy was surpassed by both formulations, with the MMC-GalG/g/PMMA@BIS system showing the most pronounced effect.

Quantitatively, the IC₅₀ values provide a clear picture of the relative potencies. Free MMC exhibited an IC₅₀ of $21 \pm 2.2 \mu\text{M}$, while the MMC-GalG/g/PMMA and MMC-GalG/g/PMMA@BIS nanogel showed IC₅₀ values of $15 \pm 1.9 \mu\text{M}$ and $8 \pm 0.9 \mu\text{M}$, respectively. These results highlight the superior cytotoxic effect of the MMC-GalG/g/PMMA@BIS nanogel, which exhibited a remarkable 2.6-fold lower IC₅₀ value compared to free MMC and a 1.8-fold lower IC₅₀ than the non-crosslinked MMC-GalG/g/PMMA formulation (Table 5).

To assess the selectivity of the MMC-GalG/g/PMMA@BIS nanogel towards cancer cells, the study was also conducted on HEK 293 cells. As shown in Fig. S5, at a 40 μM concentration, approximately 80 % of HEK 293 cells remained viable, indicating that the MMC-GalG/g/PMMA@BIS nanogel has minimal toxicity to normal cells. In contrast, the same concentration of 40 μM exhibited strong cytotoxicity in MDA-

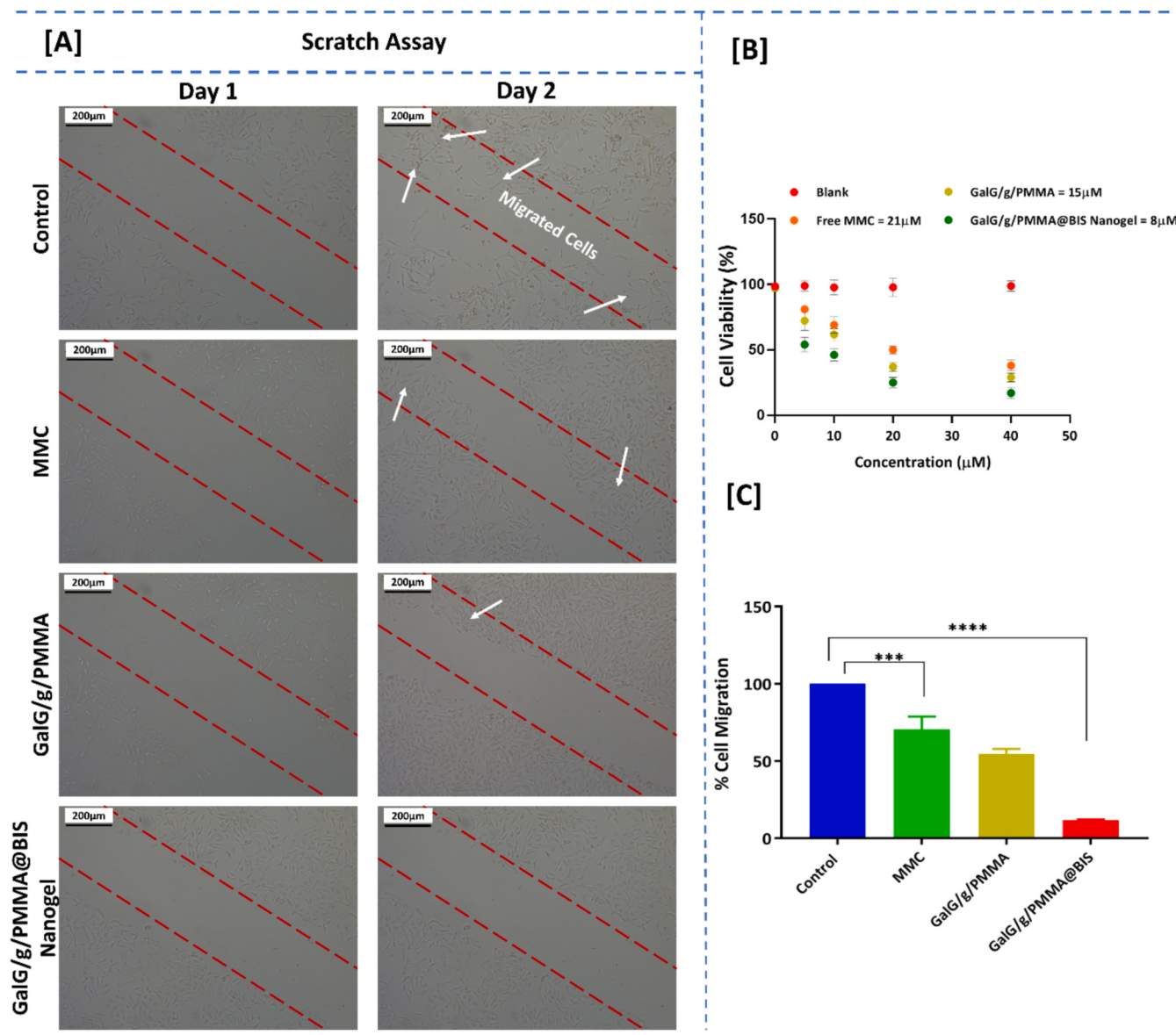


Fig. 5. Evaluation of Cell Cytotoxicity and Wound Healing Potential of Nanogels; (A) Representative microscopy images showing wound healing progression in different groups (Control, MMC-GalG/g/PMMA, MMC-GalG/g/PMMA@BIS nanogel, and MMC) at days 1 and 2. The MMC-GalG/g/PMMA@BIS nanogel group exhibited significantly reduced cell migration compared to the control group (Scale Bar 200 μm). (B) Quantitative assessment of cell migration (%) in different treatment groups. (C) Cytotoxicity analysis of different treatment groups, including control, MMC-GalG/g/PMMA, MMC-GalG/g/PMMA@BIS nanogel, and MMC. The figure highlights the dose-dependent effects of different groups on cell viability, demonstrating significantly enhanced cytotoxicity for the MMC-GalG/g/PMMA@BIS nanogel compared to MMC-GalG/g/PMMA and control... ($P_{\text{value}} < 0.001^{***}$, and $P_{\text{value}} < 0.0001^{****}$).

Table 5
IC 50 values of different groups in MDA-MB 231 cells.

Groups	IC 50 (MDA-MB 231) after 24 h.
MMC	21 ± 2.2 μM
MMC-GalG/g/PMMA	15 ± 1.9 μM
MMC-GalG/g/PMMA@BIS nanogel	08 ± 0.9 μM

Note: All MTT results were performed three times and are tabulated as the mean ± SD.

MB-231 cells, with only 17 % of the cells surviving. This significant difference underscores the nanogel's selective action, showing minimal impact on normal cells while exerting potent therapeutic effects on cancer cells.

A particularly noteworthy observation from the study was the, enhanced cytotoxicity of MMC-GalG/g/PMMA@BIS nanogel at lower doses, outperforming both free MMC and the MMC-GalG/g/PMMA formulation. This increased cytotoxic efficacy can be attributed to several factors inherent to the nanogel's design. Improved cellular uptake likely results from the nanoscale dimensions and surface properties of the MMC-GalG/g/PMMA@BIS system, facilitating more efficient internalization by cancer cells. Additionally, the redox-responsive nature of the nanogel, conferred by its disulfide crosslinks, may promote rapid drug release once internalized in the reducing intracellular milieu of cancer cells. The controlled release profile of the nanogel, as demonstrated in our previous studies, may also contribute to maintaining effective intracellular drug concentrations over the 24-h period.

To further explore the impact of different treatment groups (free MMC, MMC-GalG/g/PMMA, and, MMC-GalG/g/PMMA@BIS nanogel) on cellular function, a scratch wound assay was performed on MDA-MB 231 cells. Treatment with MMC-GalG/g/PMMA@BIS nanogel significantly reduced the wound closer rate, compared to MMC and GalG/g/PMMA treated groups [Fig. 5A]. A quantitative analysis [Fig. 5C] reveals that MMC-GalG/g/PMMA@BIS nanogel markedly reduces the cell density within the designated area, suggesting that nanogel exhibited cytotoxic effects at the marked region. The microscopic analysis [Fig. 5A] further supports these findings by demonstrating minimal cell movement and a more rounded morphology at the wound edge in the MMC-GalG/g/PMMA@BIS nanogel group. This could be due to inducing cell death (cytotoxicity) in the targeted population, leading to a decrease in overall cell number at the wound edge. These observations provide a complimentary understanding of the anti-cancer potential of nanogel. The observed results on wound closure, cell density, and cellular morphology collectively suggest that the MMC-GalG/g/PMMA@BIS nanogel not only compromises cell viability but also impairs crucial cellular processes such as proliferation and migration.

These findings complement our previous cytotoxicity data and provide a more comprehensive understanding of the anti-cancer potential of the MMC-GalG/g/PMMA@BIS nanogel. By demonstrating effects on both cell viability and functional cellular processes, our study highlights the promise of this nanogel system in potentially addressing multiple aspects of cancer progression simultaneously.

3.8.2. Cell-cycle arrest, apoptosis, and mitochondrial membrane potential (MMP) assay

Our investigation into the effects of free Mitomycin C (MMC), MMC-GalG/g/PMMA, and MMC-GalG/g/PMMA@BIS nanogel on MDA-MB 231 breast cancer cell lines yielded intriguing results across multiple cellular processes. To elucidate the mechanistic aspects of formulation's (MMC-GalG/g/PMMA, and MMC-GalG/g/PMMA@BIS nanogel), we investigated their effects on cell cycle transition, apoptosis-induction, and mitochondrial membrane potential.

Previous studies have demonstrated that MMC does not induce cell cycle arrest at specific phases but rather exerts a non-specific arrest on cell cycle progression and can inhibit cell cycle progression at any checkpoint [71]. In the cell cycle arrest assay, we observed distinct

patterns among the various treatment groups. Free MMC primarily induced arrest in the G0/G1 phase, with 66.9 % of cells accumulating in this stage. Interestingly, the MMC-GalG/g/PMMA@BIS nanogel treatment resulted in a shift towards G2/M phase arrest, with 30.7 % of cells in this phase compared to 21.4 % for GalG/g/PMMA and 17.7 % for free MMC [Fig. 6A and D]. This differential cell cycle arrest pattern suggests that the nanogel formulation may alter the cellular response to MMC, potentially by modulating its delivery or interaction with cellular targets.

Based on the evidence from the cell cycle arrest study, a quantitative determination of the apoptosis-inducing potency of the nanogel formulation was performed using a flow cytometry study based on Annexin V-FITC binding. MDA-MB-231 cells treated with MMC-GalG/g/PMMA@BIS nanogel exhibited a significantly higher apoptotic cell population compared to MMC-GalG/g/PMMA and free MMC treatments. Cells exposed to the free drug displayed approximately 25.18 % pre- and post-apoptotic cell populations. In contrast, treatment with the nanogel resulted in a total apoptotic population of 51.75 %, encompassing both early and late apoptosis stages. Additionally, cells treated with MMC-GalG/g/PMMA and free MMC showed 35.25 % and 1.33 % pre- and post-apoptotic cell populations, respectively. These findings, summarized in Fig. 6C, and F suggest that the selectively triggered programmed cell death observed may be attributed to the exploitation of the cellular internal redox environment by the nanogel system, along with its controlled release behavior.

Elevated MMP activity is linked to ECM remodeling and can induce cell cycle arrest or apoptosis in cancer cells. Healthy cells maintain high MMP for survival, but apoptotic cells exhibit decreased MMP due to mitochondrial membrane permeabilization. In apoptotic cells, the loss of MMP can be visualized by using fluorescent dyes, such as JC-1, which exhibit decreased accumulation in the mitochondria and a shift in fluorescence from red to green [72]. Our findings clearly show that MMC in either group exhibits a significant decrease in MMP [Fig. 6 B, and E] aiming to starve cancer cells to energy. The higher mitochondrial depolarization of MMC-GalG/g/PMMA@BIS nanogel (39.76 %) was observed compared to free MMC and MMC-GalG/g/PMMA groups (6.99, and 17.44 %), respectively. This higher depolarization of the mitochondrial membrane could occur due to higher apoptosis in MMC-GalG/g/PMMA@BIS nanogel-treated cells.

Collectively, these findings paint a comprehensive picture of the MMC-GalG/g/PMMA@BIS nanogel's multi-faceted anti-cancer potential. By modulating cell cycle progression, potently inducing apoptosis, and disrupting mitochondrial function, the nanogel demonstrates superior efficacy compared to free MMC and the non-crosslinked formulation (MMC-GalG/g/PMMA). These results not only support the nanogel's application as a drug delivery system, but also suggest its potential synergistic effects between the delivery mechanism and the pharmacological action of MMC.

3.8.3. Cell uptake and ROS studies

Our investigation into the intracellular cellular uptake behavior of the MMC-GalG/g/PMMA@BIS nanogel system in MDA-MB-231 cells yielded compelling results, particularly when compared to the non-crosslinked MMC-GalG/g/PMMA formulation and MMC-control treatments. These findings provide crucial insights into the nanogel's mechanism of action and its potential advantages as a drug delivery system.

Confocal laser scanning microscopy (CLSM) revealed that cells exposed with C6-GalG/g/PMMA@BIS exhibited significantly stronger green fluorescence output compared to those treated with C6-GalG/g/PMMA or the control at all observed time points [Fig. 7A; (a), (b)]. This enhanced fluorescence intensity suggests that the incorporation of disulfide linkages in C6-GalG/g/PMMA@BIS facilitates glutathione (GSH)-triggered disassembly and rapid dye release within the cellular environment. As the incubation time extended from 2 to 6 h, we observed a further increase in the intensity of green fluorescence, with

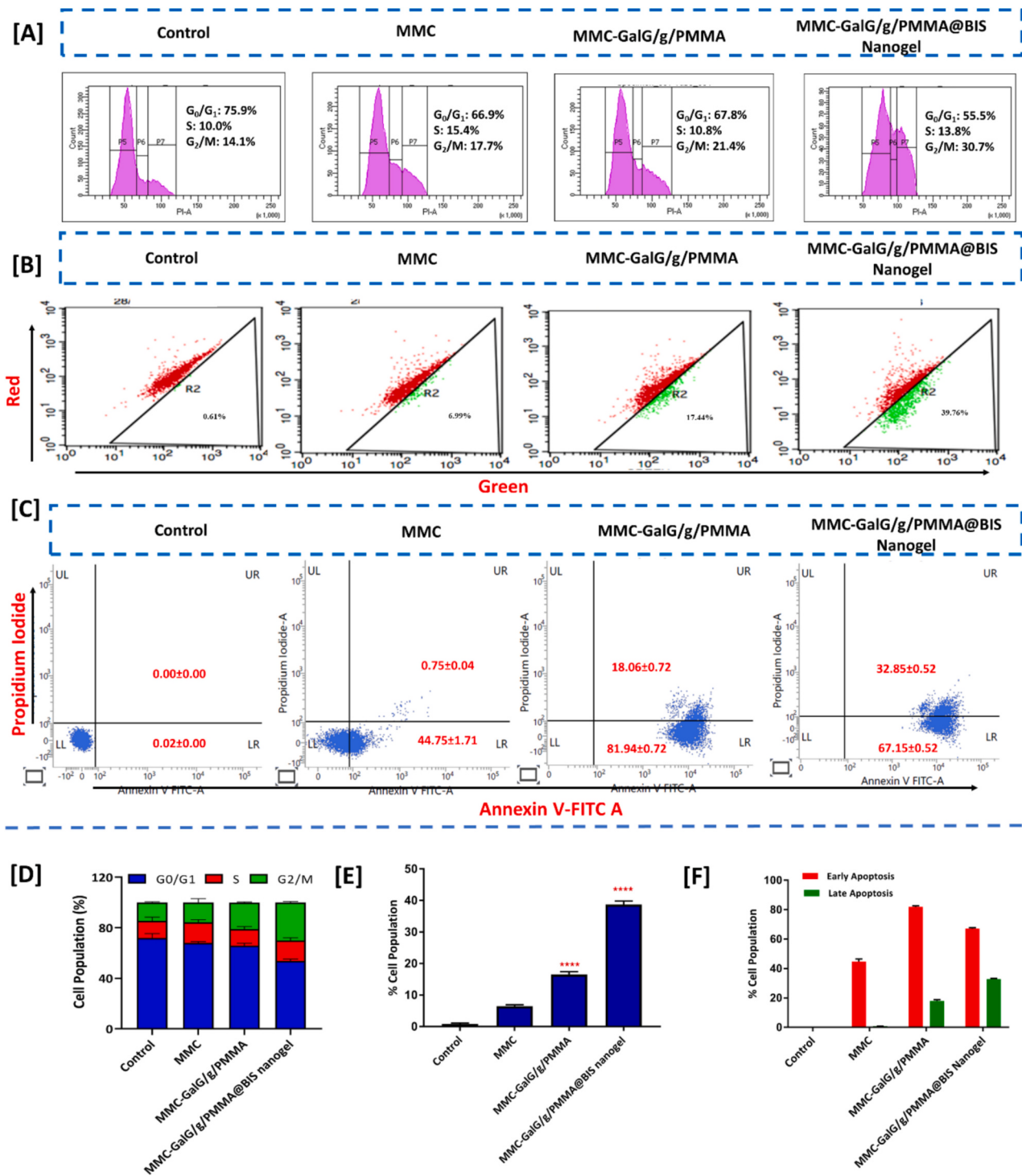


Fig. 6. [A-F] Effect of different treatment groups (control, free MMC, MMC-GalG/g/PMMA, and MMC-GalG/g/PMMA@BIS nanogel) on cell cycle distribution, MMP activity, and Annexin V-FITC apoptosis assay for 24 h. [A, D] Histogram and bar diagram depicted the flow cytometry output of cell cycle distribution following treatment with control, free MMC, MMC-GalG/g/PMMA, and MMC-GalG/g/PMMA@BIS nanogel for 24 h. [B, E] Quantification of MMP activity represented by dot plot and bar diagram. [C, F] Representative dot plots depict apoptotic cell populations in Control, Free MMC, MMC-GalG/g/PMMA, and MMC-GalG/g/PMMA@BIS nanogel groups. The percentage of post-apoptotic cells (Annexin V-positive/PI-positive) was observed as 0.00 % in the Control group, 0.75 % in the Free MMC group, 18.06 % in the MMC-GalG/g/PMMA group, and 32.85 % in the MMC-GalG/g/PMMA@BIS nanogel group, indicating enhanced apoptotic induction with cross-linked nanogel. Mean \pm standard deviation values from three independent trials are reported. ($0.001 < p < 0.05$).

notable localization in the nucleus. This time-dependent increase in fluorescence intensity due to nuclear accumulation indicates enhanced cellular uptake in addition to effective intracellular trafficking of the nanogel system.

To quantitatively corroborate these observations, we employed flow

cytometry to measure cellular uptake of the various formulations [Fig. 7C]. The results aligned closely with our CLSM findings, demonstrating significantly higher mean fluorescence intensity (MFI) in cells treated with MMC-GalG/g/PMMA@BIS compared to those exposed to MMC-GalG/g/PMMA or control treatments. This quantitative data

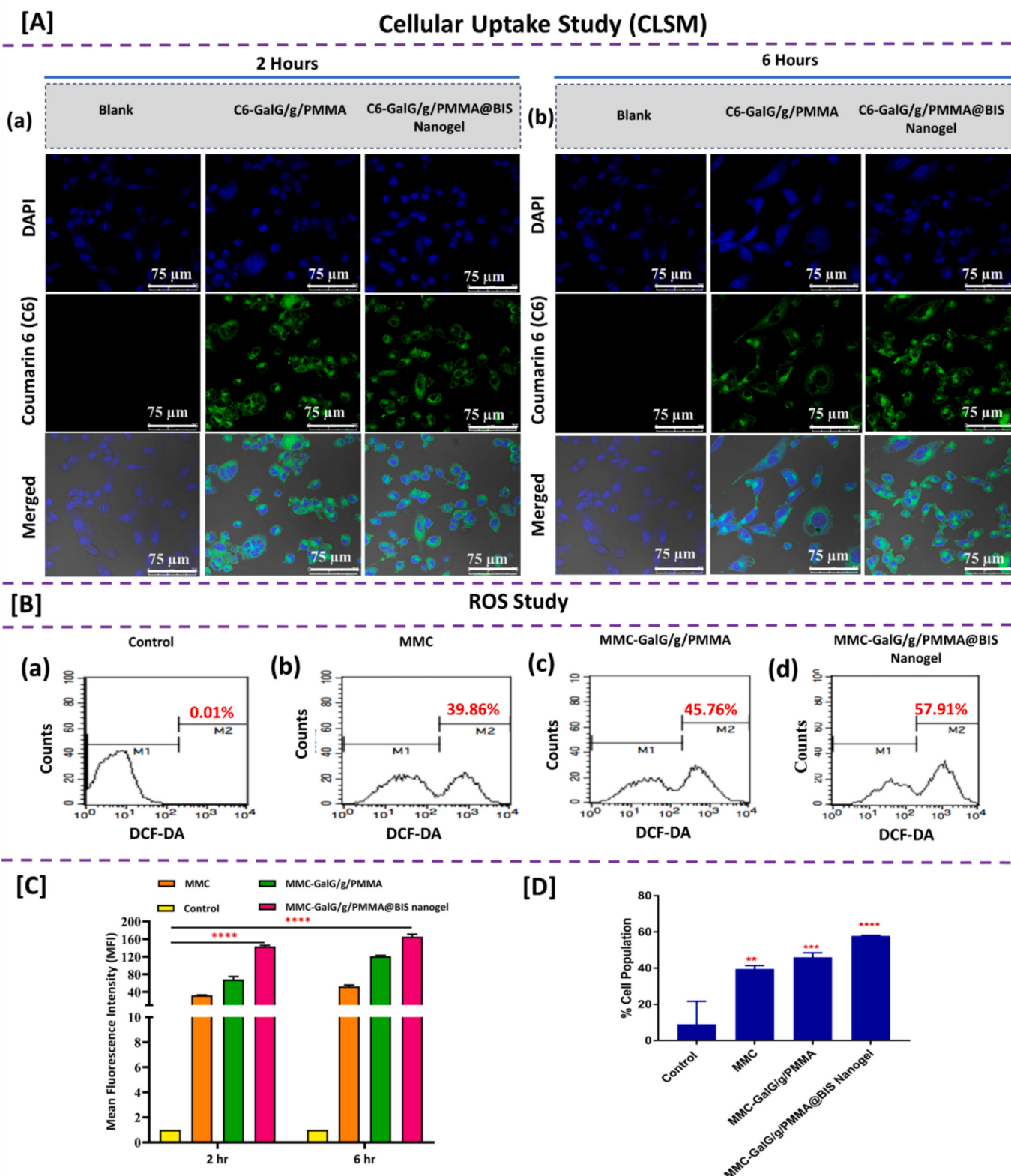


Fig. 7. [A] Intracellular uptake study by confocal imaging (CLSM) after treatment with coumarin-6(C6)-tagged formulations (control, C6-GalG/g/PMMA, and C6-GalG/g/PMMA@BIS nanogel) in MDA-MB-231 cells after (a) 2 h, and (b) 6 h (scale bar 75 μ m). [C] Quantitative uptake analysis by flow cytometry after 2 h, and 6 h hrs with control, free MMC, MMC-GalG/g/PMMA, and MMC-GalG/g/PMMA@BIS nanogel treatment [B, D] Histogram and bar diagram representing the ROS activity in MDA-MB 231 cell line after 24 h with control, free MMC, MMC-GalG/g/PMMA, and MMC-GalG/g/PMMA@BIS nanogel treatment. All the experiments were carried out in triplicate ($n = 3$). (P-value summary: $p < 0.0001^{****}$, $p < 0.001^{***}$, $p < 0.01^{**}$, $p < 0.05^*$, ns: Not significant.)

further supports the superior cellular internalization and payload release capabilities of the disulfide-crosslinked nanogel system (MMC-GalG/g/PMMA@BIS).

In parallel, we investigated the impact of our nanogel system on intracellular reactive oxygen species (ROS) production using the DCFH-DA fluorescent probe. This lipophilic, non-fluorescent dye permeates cell membranes and is converted to DCFH by cellular enzymes (esterases). In the influence of ROS, DCFH is further oxidized to the highly fluorescent 2,7-dichlorofluorescein (DCF), allowing for quantitative assessment of intracellular ROS levels. Histogram [Fig. 7B], and bar diagram [Fig. 7D] revealed that cells treated with MMC-GalG/g/PMMA@BIS nanogel exhibited significantly elevated ROS production

compared to free MMC, and MMC-GalG/g/PMMA treatments. This marked increase in ROS levels suggests that the nanogel system may exert its cytotoxic effects partly through oxidative stress induction.

Intriguingly, our findings on ROS production align with observations from our cell cycle arrest studies. Previous research has established that ROS levels tend to be elevated in cells progressing through the S and G2/M phases of the cell cycle. Our cell cycle analysis demonstrated a shift in cell population from G0/G1 towards G2/M phase in nanogel-treated cells, which could contribute to the observed increase in ROS levels across treatment groups.

The collective results from this cellular uptake and ROS production studies provide valuable insights into the mechanism of action of the

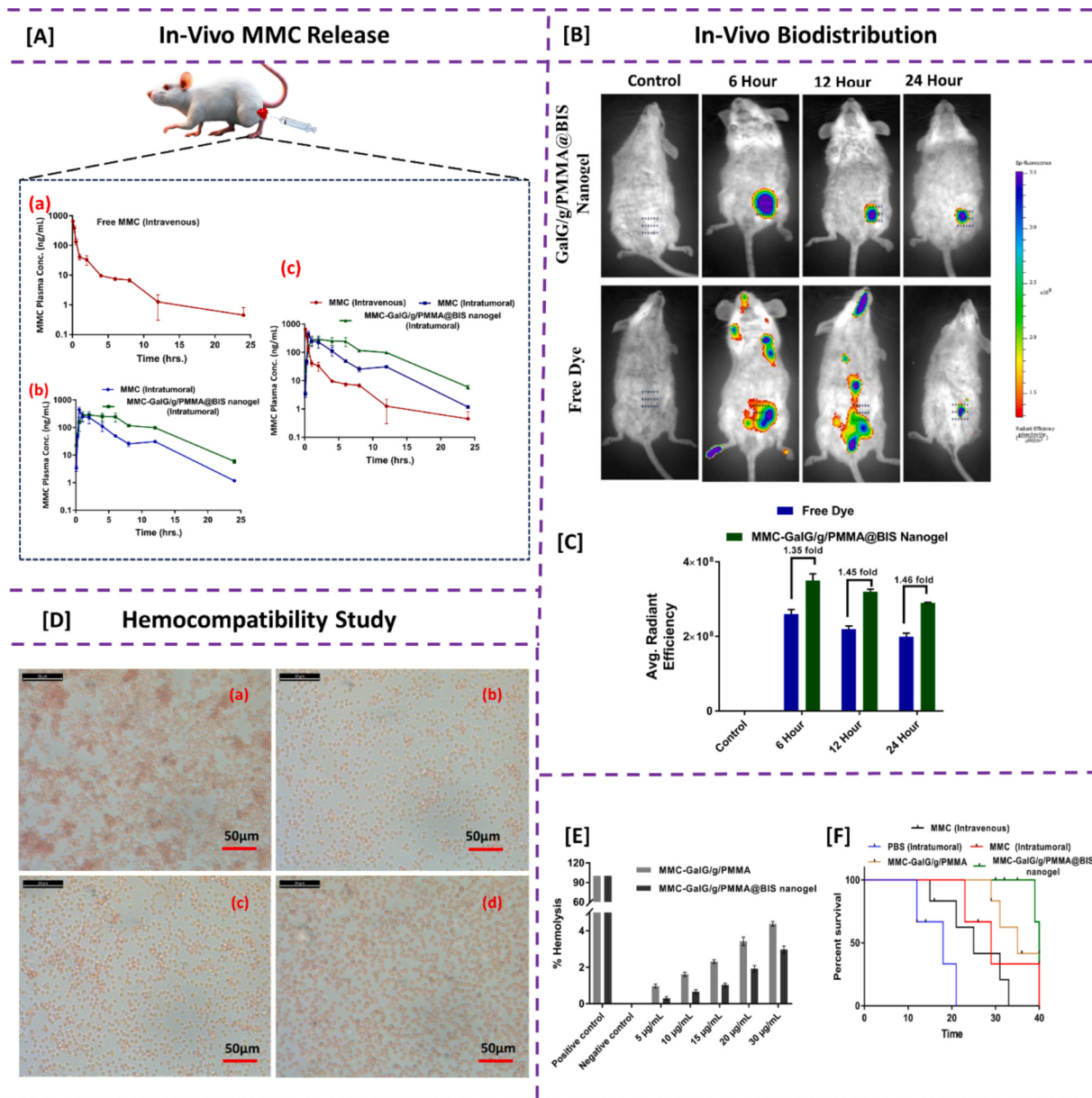


Fig. 8. [A] In-vivo MMC release, (a) Plasma exposure of MMC after intravenous injection, (b) Intratumorally inoculated with free MMC and MMC-GalG/g/PMMA@BIS nanogel, (c) Comparative PK analysis of IV, and IT injected free MMC and MMC-GalG/g/PMMA@BIS nanogel, [B, C] Qualitative and quantitative assessment of fluorescence at tumor in animals treated with free MMC and MMC-GalG/g/PMMA@BIS nanogel groups. The fluorescence intensity at tumor sites was measured at 6, 12, and 24 h following intratumoral administration. The data represent the average fluorescence intensity observed in tumor tissues at each time point. The results indicate that the GalG/g/PMMA@BIS nanogel exhibited greater accumulation in tumor tissue compared to Free dye. [D, E] Qualitative and quantitative hemocompatibility study of MMC-GalG/g/PMMA and MMC-GalG/g/PMMA@BIS nanogel ($n = 3$). [D] Blood smear images of (a) Positive control (Triton X-100), (b) Negative control (PBS), (c) MMC-GalG/g/PMMA, and (d) MMC-GalG/g/PMMA@BIS nanogel (Scale bar 50 μ m). [E], Percentage hemolysis of positive control, negative control, MMC-GalG/g/PMMA (5–30 μ g/mL), and MMC-GalG/g/PMMA@BIS nanogel (5–30 μ g/mL). [F] Survival analysis of 4T1 tumor-bearing mice administrated with PBS, free MMC, and MMC-loaded formulations (MMC-GalG/g/PMMA, and MMC-GalG/g/PMMA@BIS nanogel) ($n = 5$).

MMC-GalG/g/PMMA@BIS nanogel system. The enhanced cellular internalization, coupled with GSH-triggered disassembly and rapid payload release, suggests that the nanogel effectively exploits the reducing intracellular environment of cancer cells. Moreover, the ability to induce significant ROS production may represent an additional mechanism by which the nanogel exerts its anti-cancer effects, potentially synergizing with the cytotoxic action of the delivered MMC. These findings not only demonstrate the superior performance of the MMC-GalG/g/PMMA@BIS nanogel compared to non-crosslinked formulation (MMC-GalG/g/PMMA), but also highlight its potential as a multi-faceted anti-cancer drug delivery system.

3.8.4. Subcellular localization using Lysotracker Green

To further elucidate the intracellular fate of the nanogels, we employed CLSM to visualize their subcellular localization. Co-localization studies with Lysotracker Green, a lysosomal marker, revealed that the nanogels were trafficked to lysosomes. As shown in Fig. S6, the overlap of red fluorescence (Rhodamine) from the nanogels and green fluorescence (Lysotracker green) from Lysotracker resulted in yellow fluororescence, indicating co-localization [73,74]. This co-localization signals intensified over time, suggesting that the nanogels were progressively transported to lysosomes. (Fig. S6, Supporting Information).

3.8.5. Hemocompatibility study

Complementing the survival analysis, our hemocompatibility studies provide crucial safety data supporting the potential for intratumoral administration of the nanogel formulation. The hemolysis assay, presented in Fig. 8E, demonstrated that all tested concentrations of the nanoparticles induced <5% hemolysis, well within the acceptable range for biomedical applications. This low hemolytic activity suggests a minimal risk of red blood cell damage upon contact with the formulation, a critical consideration for intratumoral use.

Furthermore, microscopic examination of blood smears at 40 \times magnification, as shown in Fig. 8D, revealed no significant alterations in blood cell morphology for either MMC-GalG/g/PMMA or MMC-GalG/g/PMMA@BIS nanogel compared to control groups. The absence of observable changes in blood cell morphology further supports the blood compatibility of these formulations. These hemocompatibility findings are particularly important given the intended intratumoral administration route, suggesting that even if the nanogel formulation enters the bloodstream from the tumor site, it is unlikely to cause significant damage to blood cells or disrupt normal hematological function.

3.9. In-vivo study

3.9.1. MMC locoregional delivery minimizes systemic exposure in comparative pharmacokinetic evaluation

The validated UHPLC-MS/MS method (methodology in supplementary Section 2.2) was applied to trace the MMC concentrations in plasma after the single- intratumoral, or intravenous administration of MMC (4 mg/kg) ($n = 5$) in female BALB/c mice. The MMC concentrations were

quantified upto 24 h. The study compared the plasma profile of free MMC administered intravenously (IV) with that of both free and nanogel-encapsulated MMC (MMC-GalG/g/PMMA@BIS nanogel) delivered intratumorally (IT), all at a dose of 4 mg/kg.

The mean plasma concentration vs. time curves of MMC after intratumoral and intravenous delivery has been shown in Fig. 8A (a-c). The pharmacokinetic (PK) parameters were generated and are displayed in Table 6. The peak MMC plasma concentrations (Cmax) were found to be 659.10 ± 80.51 ng/mL after Intravenous and 440.33 ± 111.45 ng/mL, and 326.33 ± 32.62 ng/mL after locoregional injection for MMC and MMC-GalG/g/PMMA@BIS nanogel respectively, with observed Tmax of 0.08 ± 0.00 , 0.50 ± 0.00 , and 3.33 ± 2.31 h, respectively. The area under the MMC plasma concentration vs. time curve from 0 to 24 h (AUC(0–24 h)) was recorded to be 361.39 ± 53.98 h*ng/mL after intravenous and 1365.33 ± 301.64 h*ng/mL, and 2892.29 ± 252.72 h*ng/mL after intratumoral injections for MMC and MMC-GalG/g/PMMA@BIS nanogel, respectively. Further, the half-life ($t_{1/2}$) for MMC in all groups was found between 3 and 5 h. The observed apparent systemic clearance (Cl/F_{obs}) values were determined to be 0.011 ± 0.002 for IV, and 0.003 ± 0.001 , 0.001 ± 0.000 (mg)/(ng/mL)/h for MMC and MMC-GalG/g/PMMA@BIS nanogel delivered intratumorally, respectively. These values suggest significantly different drug elimination rates among the groups, with the IV group exhibiting the highest and MMC-GalG/g/PMMA@BIS nanogel with IT delivery showing the lowest clearance.

Pharmacokinetic analysis revealed a significantly higher maximum plasma concentration (Cmax) of free Mitomycin C (MMC) following intravenous (IV) administration compared to the nanogel formulation delivered intratumorally (IT). Specifically, the Cmax of free MMC after IV administration was approximately 2.02-fold greater than the Cmax of MMC released from the nanogel delivered intratumorally. Additionally, the Cmax of free MMC after IV administration was roughly 1.50-fold higher compared to the Cmax of free MMC following IT administration. These findings suggest that the intratumoral delivery of the nanogel formulation significantly reduces systemic exposure to MMC compared to MMC administered intravenously. In the context of IT delivery, a lower Cl/F_{obs} value, as observed in the MMC-GalG/g/PMMA@BIS nanogel group, suggests prolonged drug retention, reduced systemic exposure, and enhanced intratumoral efficacy. The AUC of the drug was determined to be 361.39 ± 53.98 h*ng/mL after intravenous (IV) administration of MMC and 2892.29 ± 252.72 h*ng/mL for MMC-GalG/g/PMMA@BIS nanogel delivered intratumorally. This suggests prolonged drug retention at the tumor site following IT delivery compared to systemic administration.

Our pharmacokinetic findings exhibited several positive and striking observations. The significantly lower Cmax observed with IT delivery of the nanogel formulation (approximately 2.02-fold lower than IV MMC) suggests a substantial reduction in systemic MMC exposure. This reduction likely translates to decreased systemic toxicity; a critical consideration given MMC's known side effects. Further, the higher AUC achieved with the nanogel formulation, despite lower peak concentrations, indicates sustained release of MMC at the tumor site. This

Table 6

Pharmacokinetic parameters of different groups.

PK parameter	Unit	Intravenous (IV)	Intratumoral (IT)	MMC-GalG/g/PMMA@BIS Nanogel
		MMC	MMC	
Tmax	h	0.08 ± 0.00	0.50 ± 0.00	3.33 ± 2.31
Cmax	ng/mL	659.99 ± 80.51	440.33 ± 111.45	326.33 ± 32.62
T _{1/2}	h	4.07 ± 1.20	3.08 ± 0.252	3.42 ± 0.20
AUC _{0-last}	h*ng/mL	361.39 ± 53.98	1365.33 ± 301.64	2892.29 ± 252.72
MRT	h	2.13 ± 0.523	4.79 ± 0.51	6.90 ± 0.30
Cl/F _{obs}	(mg)/(ng/mL)/h	0.011 ± 0.002	0.003 ± 0.001	0.001 ± 0.000

Note: Cmax: maximum plasma MMC concentration; Tmax: time to reach maximum MMC concentration; AUC_{0-last}: area under the MMC plasma concentration-time curve over the last hours; T_{1/2}: half-life; MRT: mean residence time, Cl/F_{obs}: apparent systemic clearance following extravascular administration.

prolonged exposure may enhance therapeutic efficacy by maintaining effective drug concentrations over an extended period. Therefore, combining reduced systemic exposure (lower Cmax) with enhanced local drug delivery (higher AUC), our nanogel formulation potentially offers an improved therapeutic index compared to conventional IV administration of MMC. The ability to achieve therapeutic drug levels through IT administration opens up new possibilities for localized cancer therapy. These results underscore the potential of the MMC-GalG/g/PMMA@BIS nanogel as an innovative drug delivery system for MMC in cancer therapy. By modulating the pharmacokinetic profile of MMC, our approach may allow for more effective and safer treatment strategies.

3.9.2. Nanogel prolongs survival in animals

The Kaplan-Meier survival analysis, illustrated in Fig. 8F, reveals striking differences in survival outcomes among the treatment groups, with the MMC-GalG/g/PMMA@BIS nanogel demonstrating the most impressive survival benefit. Animals treated with this formulation exhibited a median survival exceeding 40 days (% survival ~70 %), significantly outperforming all other treatment groups. The non-crosslinked MMC-GalG/g/PMMA formulation showed improved survival (35 days) compared to free MMC treatments but fell short of the crosslinked nanogel's performance. Intra-tumoral administration of free MMC resulted in a median survival of 29 days (% survival ~30 %), while intravenous free MMC (% survival ~16 %) showed the shortest median survival of 25 days with complete mortality within the 40-day study period.

These survival data align closely with our pharmacokinetic findings, suggesting that the enhanced survival in the nanogel-treated group likely stems from a combination of factors. These include reduced systemic exposure due to localized drug delivery and controlled release, prolonged exposure to therapeutic drug concentrations at the tumor site, and potential synergistic effects between the nanogel's properties and MMC's mechanism of action.

3.9.3. In vivo optical imaging in 4T1 xenografted mice

Our investigation into the biodistribution of the MMC-GalG/g/PMMA@BIS nanogel within tumor sites has yielded compelling insights into its potential for targeted and sustained drug delivery in local cancer therapy. We conducted this study using Balb/c mice bearing 4T1-induced tumors, comparing the distribution patterns of our nanogel loaded with Evans blue dye (GalG/g/PMMA@BIS nanogel) to that of a free dye solution.

Utilizing the Caliper-IVIS (Kinetic In Vivo Optical Imaging System), we captured fluorescence images at 6-, 12-, and 24-hours post-administration to assess nanogel localization within the tumors. The results, as illustrated in Fig. 8B, reveal striking differences in the spatiotemporal distribution patterns between the nanogel formulation (GalG/g/PMMA@BIS nanogel) and free dye.

The nanogel demonstrated remarkable localized accumulation and prolonged retention within the tumor tissues. This observation is particularly significant as it suggests that our nanogel system can effectively concentrate at the target site, potentially enhancing therapeutic efficacy while minimizing systemic exposure to drug. In contrast, the free dye treatment groups exhibited rapid and widespread distribution throughout the body, with minimal intratumoral accumulation.

Quantitative analysis (Fig. 8C) of the fluorescence intensity (in terms of radiance) further supports the qualitative observations. The GalG/g/PMMA@BIS nanogel formulation demonstrated a significant retention in tumor-specific fluorescence intensity at each time point. In comparison, the free dye group exhibited much lower fluorescence intensity, indicating less tumor accumulation and slower retention over time. At the 6-hour mark, the GalG/g/PMMA@BIS nanogel had a noticeable increase in fluorescence compared to free MMC, reflecting the enhanced accumulation of the nanogel formulation by the tumor. At 12 and 24 h, the disparity became more evident, with the GalG/g/PMMA@BIS nanogel maintaining consistently higher fluorescence intensity in the

tumor region, while the fluorescence signal of the free dye significantly decreased. This suggests that the GalG/g/PMMA@BIS nanogel formulation offers prolonged retention and accumulation within the tumor, likely due to its nanogel-based drug delivery system, which enhances the stability and bioavailability of the drug at the tumor site.

A key finding from our analysis is the superior penetration depth achieved by the nanogel within tumor tissues compared to free dye. This enhanced penetration capability is critical, as it suggests that our nanogel formulation can potentially access regions of the tumor that may be inaccessible to freely diffusing molecules. Such deep penetration could lead to more comprehensive treatment of the entire tumor mass, addressing issues of heterogeneity and drug resistance often encountered in solid tumors.

These biodistribution findings align closely with our previous in vivo pharmacokinetic studies, providing further validation of the nanogel's efficacy in tumor targeting. The ability of our nanogel system to achieve localized accumulation, deep tissue penetration, and sustained retention addresses several key challenges in cancer drug delivery. The corollaries of these results are far-reaching. By enabling more precise targeting of tumor tissues, our nanogel formulation could potentially enhance the therapeutic index of encapsulated drugs, allowing for higher local concentrations while minimizing systemic toxicity. The observed sustained retention could translate to improved treatment efficacy and potentially reduced dosing frequency, enhancing patient compliance and quality of life.

3.9.4. Tumor regression studies

Our evaluation of the MMC-GalG/g/PMMA@BIS nanogel's anti-cancer efficacy against a triple-negative breast cancer (TNBC) model in mice has yielded remarkably promising results, demonstrating significant advantages over conventional treatments. The tumor volume measurements, as illustrated in Fig. 9C, provide compelling evidence of the nanogel's superior therapeutic efficacy. The tumor volume data reveals distinct variations in tumor progression among the treatment groups over 21 days. The control group showed rapid tumor growth, reflecting aberrant tumor proliferation in the absence of treatment. The MMC-treated group showed a moderate reduction in tumor growth compared to the control, indicating partial therapeutic efficacy. The MMC-GalG/g/PMMA group demonstrated significantly better tumor control, suggesting enhanced drug retention. Remarkably, the MMC-GalG/g/PMMA@BIS nanogel group exhibited the most pronounced therapeutic effect, with tumor volume decreasing substantially from 76 mm³ to 17 mm³, highlighting the superior efficacy of the targeted formulation in inhibiting tumor progression and inducing regression, likely due to precise targeting and efficient drug delivery.

Further corroborating these findings, the analysis of excised tumor weights at the study's conclusion revealed even more striking differences. As shown in Fig. 9D, tumors from the MMC-GalG/g/PMMA@BIS nanogel-treated group were 7.87-fold lighter than those from the saline control, MMC-GalG/g/PMMA group showed a 5.62-fold decrease in tumor weight, indicating a moderate but notable reduction in tumor growth when compared to control. The consistency between tumor volume and weight measurements provides robust evidence of the nanogel's therapeutic efficacy. Moreover, the photographic illustration of harvested tumors in Fig. 9B (a) visually confirms these quantitative findings, aligning well with our in vitro cytotoxicity results.

Importantly, our study also addressed the critical aspect of treatment safety and tolerability. Body weight monitoring, as depicted in Fig. 9E, revealed that mice treated with free MMC experienced notable weight loss, a common indicator of systemic toxicity. In contrast, both formulations (MMC-GalG/g/PMMA@BIS and MMC-GalG/g/PMMA nanogel) demonstrated not only increased efficacy but also good tolerability, with body weight increases similar to the control group. This observation suggests that the nanogel formulations may offer a wider therapeutic window, potentially allowing for more aggressive treatment regimens with reduced side effects.

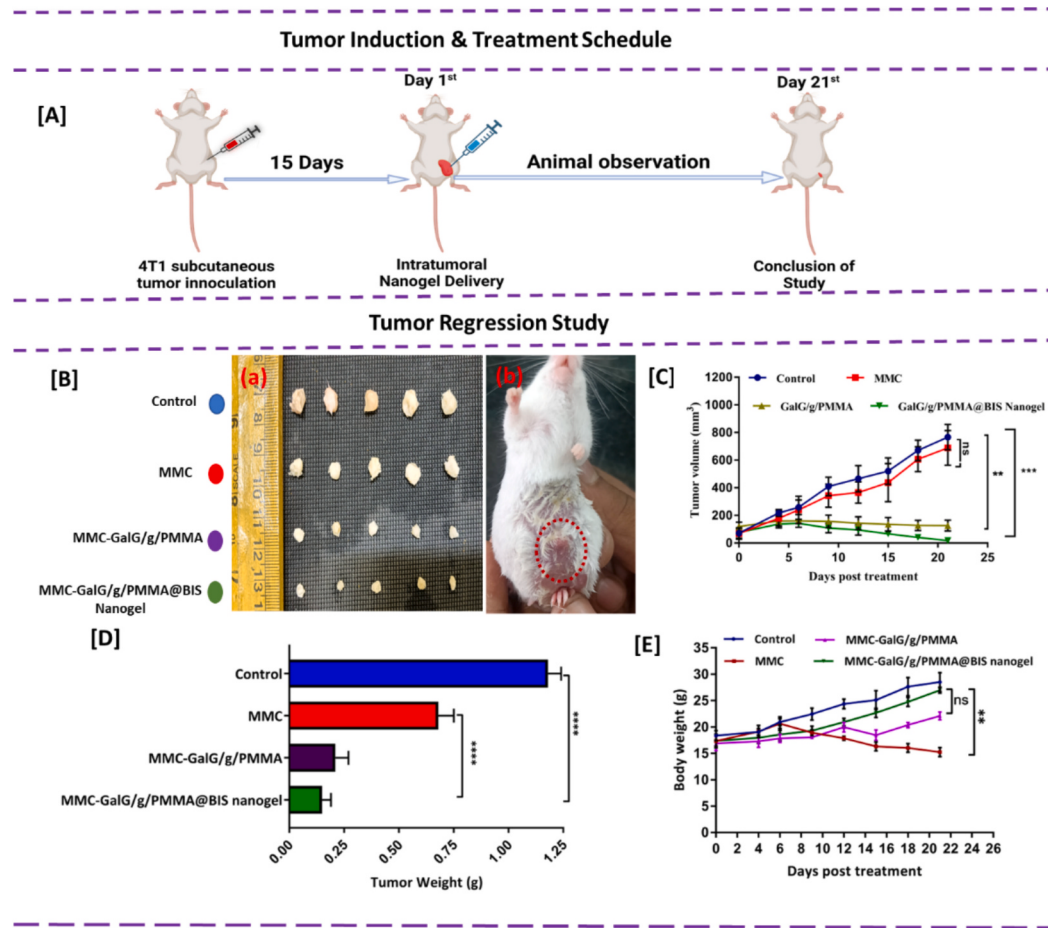


Fig. 9. Evaluation of antitumor efficacy using a 4T1 mammary tumor xenograft model in BALB/c mice with the dose of MMC (4 mg/kg). [A] In-vivo tumor induction and nanogel treatment schedule, [B] Photographs showing the morphology of harvested tumors at the termination of the study (a), Tumor-bearing mice (b), [C] tumor volume, [D] tumor weight, [E] body mass/weight of tumor-xenografted mice recorded throughout the study period. All data values are represented as mean \pm SD ($n = 5$ in all treatment groups); P value summary: $p < 0.0001^{***}$, $p < 0.001^{**}$, $p < 0.01^{**}$, $p < 0.05$, ns: Not significant.

The superior antitumor efficacy of the MMC-GalG/g/PMMA@BIS nanogel can be attributed to a combination of favorable characteristics, including an optimized pharmacokinetic profile, potent cytotoxicity, sustained intracellular drug release, and enhanced in vivo performance. These properties, demonstrated in our earlier studies, collectively contribute to the nanogel's ability to maintain therapeutic drug concentrations within the tumor microenvironment while minimizing systemic exposure. By demonstrating superior tumor growth inhibition coupled with improved tolerability through MMC-GalG/g/PMMA@BIS nanogel, this holds significant promise for advancing cancer therapy and potentially improving outcomes for patients with this challenging form of breast cancer.

3.10. Histology

Our comprehensive evaluation of the MMC-GalG/g/PMMA@BIS nanogel's in vivo performance extended to a detailed histological analysis, providing crucial insights into its therapeutic efficacy. The analysis based on tissue sections stained with hematoxylin and eosin (H&E), as shown in Fig. 10 [A, B] yielded compelling evidence supporting the nanogel's potential as an effective drug delivery system for cancer treatment. Notably, the histological analysis of tumor tissues revealed marked differences among the treatment groups. Tumors treated with the MMC-GalG/g/PMMA@BIS nanogel exhibited a markedly disrupted and necrotic morphology, compared to the saline control, free MMC, and MMC-GalG/g/PMMA treated groups [Fig. 10B]. This alteration in tumor tissue architecture is indicative of potent therapeutic

effects and aligns with our observations of reduced tumor volume and weight in the nanogel-treated group. [75]

The 4T1 model is widely recognized as a standard for studying breast cancer due to its highly metastatic characteristics, closely resembling the progression of human breast cancer. These cells spontaneously metastasize from the primary tumor to distant organs, such as the lungs [76]. After 21 days of treatment with saline control, free MMC, MMC-GalG/g/PMMA, or MMC-GalG/g/PMMA@BIS nanogel, mice were sacrificed, and lung tissues were subjected to H&E staining. The control and free MMC groups exhibited significant lung metastasis, as evidenced by the presence of large metastatic nodules (redhead arrow, [Fig. 10A]). The MMC-GalG/g/PMMA group showed a mild reduction in metastasis. In contrast, the MMC-GalG/g/PMMA@BIS nanogel group demonstrated a significant inhibition of lung metastasis, with no visible metastatic nodules [Fig. 10A]. These results highlight the potential of nanogel therapy in preventing distant metastasis and improving overall survival.

3.11. Immunohistochemistry studies (Ki67)

To assess the impact of different treatment groups on cell proliferation, immunofluorescence staining for Ki-67 was conducted on formalin-fixed, paraffin-embedded (FFPE) tumor tissue sections. Confocal microscopy was used to visualize and quantify Ki-67 protein expression. As illustrated in Fig. 10C, the control group displayed a high number of Ki-67-positive cells, reflecting substantial proliferative activity. In contrast, treatment with GalG/g/PMMA and GalG/g/PMMA@BIS nanogel led to a notable decrease in Ki-67-positive cells, indicating a strong inhibition

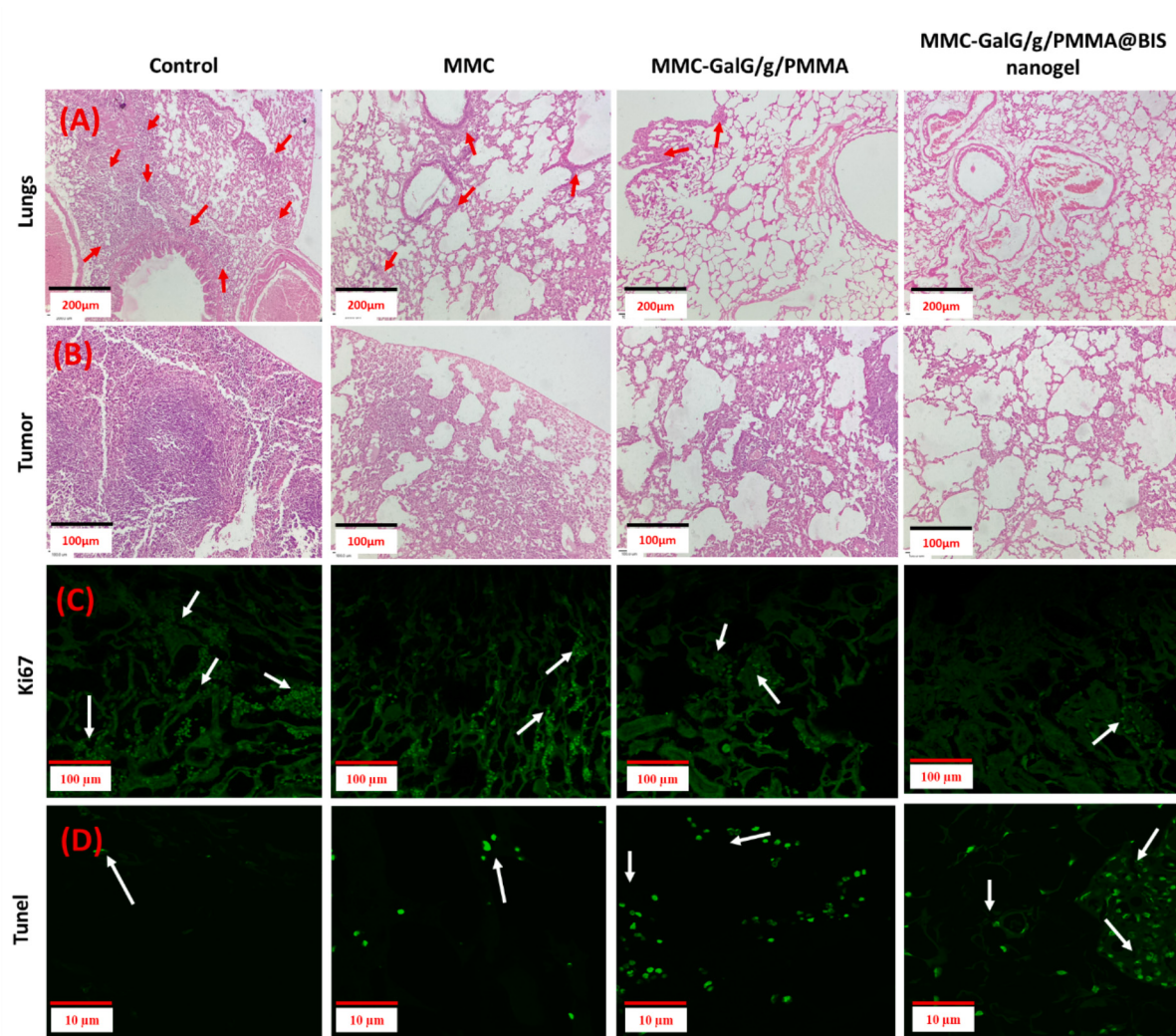


Fig. 10. Anti-metastasis activity of nanogel to the lungs. (A) H&E-stained images of lung tissues from mice treated with saline (control), free MMC, MMC-GalG/g/PMMA, and MMC-GalG/g/PMMA@BIS nanogel formulations. Red arrowheads mark metastatic nodules in the lung tissue. (Scale bar = 200 μ m). (B) Hematoxylin and Eosin (H&E) Staining of Tumor Tissues Across Treatment Groups. Tumor sections from Control, Free MMC, MMC-GalG/g/PMMA, and MMC-GalG/g/PMMA@BIS nanogel groups. The control group shows dense cellularity with minimal necrosis. Free MMC-treated tumors exhibit moderate apoptosis and necrosis. MMC-GalG/g/PMMA-treated tumors show enhanced necrosis, while MMC-GalG/g/PMMA@BIS nanogel-treated tumors display extensive necrosis and disrupted architecture, indicating superior therapeutic efficacy (Scale bar = 100 μ m). (C, D) Confocal microscopy images of (C) Ki-67 immunofluorescence staining and (D) TUNEL assay for apoptosis, showing tumor cell proliferation and apoptosis, respectively, across the four treatment groups: Control, MMC, MMC-GalG/g/PMMA, and MMC-GalG/g/PMMA@BIS nanogel (Scale bar = 100 μ m). (C) Ki-67 staining shows the proliferation marker in green, with a higher number of Ki-67-positive cells observed in the Control group and a marked reduction in the MMC-GalG/g/PMMA, and MMC-GalG/g/PMMA@BIS nanogel groups, indicating decreased cell proliferation, white arrowheads mark proliferative cell (D) TUNEL assay images reveal apoptotic cells in green, showing minimal apoptosis in the Control group, a moderate increase in MMC and MMC-GalG/g/PMMA groups, and a pronounced increase in apoptotic cells in the MMC-GalG/g/PMMA@BIS nanogel group, reflecting enhanced apoptosis. Nuclei were stained with DAPI (blue). white arrowheads mark apoptotic cells (Scale bar = 10 μ m). (For interpretation of the references to colour in this figure legend, the reader is referred to the web version of this article.)

of cell proliferation. The free MMC group showed a moderate reduction in Ki-67 expression.

3.12. TUNEL assay

TUNEL assay results (Fig. 10D) revealed that the MMC-loaded GalG/g/PMMA@BIS nanogel induced the highest level of apoptosis, followed by MMC-loaded GalG/g/PMMA formulation and free MMC. This suggests that the nanogel delivery approach significantly enhances the therapeutic efficacy of MMC. These findings are consistent with Annexin V FITC apoptosis assay, which measures early apoptotic events. Both assays demonstrate the superiority of targeted nanocarriers in delivering the drug to tumor cells and inducing cell death.

4. Conclusion

In this study, we have successfully developed a novel intratumoral drug delivery system based on gellan gum (GalG), a natural polysaccharide. To enhance the responsiveness of the system to the tumor microenvironment, we incorporated a redox-sensitive cross-linker, BIS, into the GalG matrix. This approach resulted in the formation of a redox-sensitive GalG-based nanogel (MMC-GalG/g/PMMA@BIS) through a free radical polymerization process. The optimized MMC-GalG/g/PMMA@BIS nanogel, demonstrated a well-defined size of 123.37 ± 0.98 nm with a narrow size distribution ($PDI = 0.15 \pm 0.01$), indicating a uniform population that is crucial for consistent drug delivery. This homogeneity ensures predictable pharmacokinetics and therapeutic efficacy. To illustrate the practical application of our findings, we

investigated the loading of MMC, a widely used chemotherapeutic agent, into GalG/g/PMMA@BIS nanogel. We optimized the nanogel-to-drug ratios and found that a 2:1 ratio was most effective, achieving a drug loading efficiency of 45.85 % (w/w) while maintaining excellent nanogel stability. In vitro and in vivo studies demonstrated sustained MMC release from the optimized nanogels, leading to significant tumor growth inhibition with minimal systemic toxicity.

Comprehensive characterization through FTIR, NMR, and elemental analysis confirmed the successful cross-linking and grafting within the nanogel matrix. XRD analysis showed a reduction in crystallinity, indicating the formation of a robust network structure conducive to controlled drug release, providing a deeper mechanistic understanding of the nanogel system. The nanogel exhibited excellent stability under various storage conditions, including temperature variations, as well as physiological stability in different environments, highlighting its practical viability and ensuring the reliability of the developed formulation. Our findings demonstrate the successful design and characterization of a redox-sensitive nanogel system. The nanogel exhibited pronounced redox responsiveness, releasing 70–80 % of its payload in a reductive environment, mimicking the intracellular milieu, compared to only 13 % under non-reductive conditions. This selective release profile confirms the nanogel's potential for targeted intracellular drug delivery. Furthermore, the presence of plasma proteins in a simulated physiological environment under reductive conditions significantly enhanced drug release, suggesting a potential synergistic interaction with biological components. This observation highlights the nanogel's adaptability to complex biological settings, which is crucial for achieving optimal therapeutic efficacy *in vivo*. These results provide a strong foundation for further development and preclinical evaluation of this redox-sensitive nanogel platform for targeted cancer therapy. The cytotoxicity studies revealed the selective targeting ability of the nanogel, displaying significant cytotoxic effects against MDA-MB-231 cancer cells while causing minimal toxicity to healthy HEK-293 cells. Subcellular localization studies revealed that the nanogels were trafficked to lysosomes, confirming their ability to mediate intracellular drug delivery.

The MMC-GalG/g/PMMA@BIS nanogel demonstrated superior intratumoral release of the anticancer drug Mitomycin C (MMC) compared to other treatment modalities. In the MDA-MB-231 TNBC breast cancer cell line, we observed significant intracellular accumulation of the nanogel. This accumulation led to a cascade of cellular effects, including cell cycle arrest, disruption of mitochondrial membrane potential, and ultimately, induction of apoptosis. Fluorescence imaging provided valuable insights into the spatiotemporal distribution of our nanogel. The MMC-GalG/g/PMMA@BIS formulation exhibited a distinct pattern of localized accumulation and prolonged retention within the tumor site. This localized delivery approach offers a significant advantage over traditional intravenous administration of free MMC by reducing systemic drug exposure, potentially minimizing off-target effects.

Building upon the promising in-vitro results the in-vivo study aimed to evaluate the therapeutic efficacy and safety of MMC-GalG/g/PMMA@BIS nanogel in a preclinical animal model (murine xenograft breast cancer). The MMC-GalG/g/PMMA@BIS nanogel demonstrated superior antitumor efficacy, evidenced by a significant reduction in tumor volume. Importantly, MMC-GalG/g/PMMA@BIS nanogel demonstrated a favorable safety profile, with no significant changes observed in body weight throughout the treatment period, indicating minimal systemic toxicity.

Histological analysis of tumor tissue revealed significant disruption of tumor architecture, which was further supported by TUNEL and Ki67 proliferation assays. These results align with the therapeutic outcomes, demonstrating the MMC-GalG/g/PMMA@BIS nanogel's ability to compromise tumor integrity and suppress cell proliferation. Additionally, histological evaluation of lung tissues confirmed that the nanogel effectively inhibited 4T1 metastasis to the lungs. This finding is

particularly significant as it highlights the nanogel's potential not only in controlling primary tumor growth but also in preventing metastatic progression, which is a critical challenge in cancer treatment. These outcomes emphasize the nanogel's therapeutic promise in managing both localized and metastatic disease.

The improved antitumor efficacy of MMC-GalG/g/PMMA@BIS may be attributed to combination of factors. The superior pharmacokinetic profile and higher tumor accumulation, possibly due to enhanced permeability and retention (EPR) effect combined with cell-mediated uptake and nanogel-directed intracellular drug release over an extended period could be the possible reason of improved therapeutic outcome. These findings represent a significant step forward in achieving improved chemotherapeutic outcome in breast cancer treatment. The MMC-GalG/g/PMMA@BIS nanogel's ability to combine targeted delivery, controlled release, and enhanced efficacy opens new avenues for improving patient outcomes.

Future prospects

The redox-responsive intratumoral nanogels represent a promising approach for improving cancer treatment. Future research efforts focused on optimizing nanogel design, and exploring combination therapies are likely to further advance this field.

CRediT authorship contribution statement

Nikhil Rai: Writing – review & editing, Writing – original draft, Visualization, Validation, Software, Methodology, Investigation, Formal analysis, Data curation, Conceptualization. **Disha Marwaha:** Writing – review & editing, Visualization, Validation, Methodology. **Shalini Gautam:** Writing – review & editing, Visualization, Validation, Methodology. **Ravi Prakash Shukla:** Writing – review & editing, Visualization, Validation, Methodology. **Madhu Sharma:** Writing – review & editing, Visualization, Validation, Methodology. **Neha Singh:** Writing – review & editing, Visualization, Validation, Methodology. **Pratiksha Tiwari:** Writing – review & editing, Visualization, Validation, Methodology. **Sandeep Urandur:** Writing – review & editing, Visualization, Methodology. **Venkatesh Banala Teja:** Writing – review & editing, Visualization, Methodology. **Sachin Nasik Sanap:** Writing – review & editing, Visualization. **Krishna Yadav:** Writing – review & editing, Visualization. **Avijit Kumar Bakshi:** Writing – review & editing, Visualization. **Prabhat Ranjan Mishra:** Writing – review & editing, Visualization, Validation, Supervision, Software, Resources, Project administration, Methodology, Funding acquisition, Conceptualization.

Ethical statement

The animal studies for this research were planned and performed in accordance with the ethical framework of the Committee for the Purpose of Control and Supervision of Experiments on Animals (CCSEA, formerly known as CPSEA), a regulatory authority established under the Prevention of Cruelty to Animals (PCA) Act of 1960. We have ensured that our animal research practices align with internationally recognized ethical guidelines (ARRIVE guidelines) [77].

Declaration of competing interest

The authors declare that they have no known competing financial interests or personal relationships that could have appeared to influence the work reported in this paper.

Acknowledgments

The authors gratefully acknowledge the support of the Council of Scientific and Industrial Research-Central Drug Research Institute (CSIR-CDRI) and the Academy of Scientific and Innovative Research

(AcSIR), Ghaziabad, for providing essential resources and support throughout this research. We are also indebted to the National Institute of Pharmaceutical Education and Research (NIPER), Raebareli, for granting us access to their IVIS imaging facility. We sincerely thank the THUNDER (BSC0102) and MoES (GAP0118) grants for Intravital Facility of the CSIR-CDRI, SAIF Division for their support in conducting the confocal imaging studies. The authors extend their gratitude to Dr. K. Mitra for providing electron microscope facility at the Division of Electron Microscopy, CSIR-CDRI. The CSIR-CDRI communication number allotted for this manuscript is 10922.

Appendix A. Supplementary data

Supplementary data to this article can be found online at <https://doi.org/10.1016/j.ijbiomac.2025.140306>.

Data availability

Data will be made available on request.

References

- [1] M. Arnold, E. Morgan, H. Rungay, A. Mafra, D. Singh, M. Laversanne, J. Vignat, J. Ralow, F. Cardoso, S. Siesling, I. Soerjomataram, Current and future burden of breast cancer: global statistics for 2020 and 2040, *Breast* 66 (2022) 15–23, <https://doi.org/10.1016/j.breast.2022.08.010>.
- [2] S. Mubarik, R. Sharma, S.R. Hussain, M. Iqbal, X. Nawsherwan, C. Yu Liu, Breast Cancer mortality trends and predictions to 2030 and its attributable risk factors in east and south Asian countries, *Front. Nutr.* 9 (2022), <https://doi.org/10.3389/fnut.2022.847920>.
- [3] A. Hosseinpour, M. Soltani, M. Souri, Improving tumor treatment through intratumoral injection of drug-loaded magnetic nanoparticles and low-intensity ultrasound, *Sci. Rep.* 14 (2024) 1452, <https://doi.org/10.1038/s41598-024-52003-9>.
- [4] C. Chun, S.M. Lee, C.W. Kim, K.-Y. Hong, S.Y. Kim, H.K. Yang, S.-C. Song, Doxorubicin–polyphosphazene conjugate hydrogels for locally controlled delivery of cancer therapeutics, *Biomaterials* 30 (2009) 4752–4762, <https://doi.org/10.1016/j.biomaterials.2009.05.031>.
- [5] J.W. Luo, T. Zhang, Q. Zhang, X. Cao, X. Zeng, Y. Fu, Z.R. Zhang, T. Gong, A novel injectable phospholipid gel co-loaded with doxorubicin and bromotetrandrine for resistant breast cancer treatment by intratumoral injection, *Colloids Surf. B: Biointerfaces* 140 (2016) 538–547, <https://doi.org/10.1016/j.colsurfb.2015.11.029>.
- [6] A.M. Al-Abd, K.Y. Hong, S.C. Song, H.J. Kuh, Pharmacokinetics of doxorubicin after intratumoral injection using a thermosensitive hydrogel in tumor-bearing mice, *J. Control. Release* 142 (2010) 101–107, <https://doi.org/10.1016/j.jconrel.2009.10.003>.
- [7] S. Gautam, D. Marwaha, N. Singh, N. Rai, M. Sharma, P. Tiwari, S. Urandur, R. P. Shukla, V.T. Banala, P.R. Mishra, Self-assembled redox-sensitive polymeric nanostructures facilitate the intracellular delivery of paclitaxel for improved breast Cancer therapy, *Mol. Pharm.* 20 (2023) 1914–1932, <https://doi.org/10.1021/acs.molpharmaceut.2c00673>.
- [8] L. Sun, H. Liu, Y. Ye, Y. Lei, R. Islam, S. Tan, R. Tong, Y.B. Miao, L. Cai, Smart nanoparticles for cancer therapy, *Signal Transduct. Target. Ther.* 8 (2023), <https://doi.org/10.1038/s41392-023-01642-x>.
- [9] P. Liu, L. Hao, M. Liu, S. Hu, Glutathione-responsive and -exhausting metal nanomedicines for robust synergistic cancer therapy, *Front. Bioeng. Biotechnol.* 11 (2023), <https://doi.org/10.3389/fbioe.2023.1161472>.
- [10] A. Koyyada, P. Orsu, Natural gum polysaccharides as efficient tissue engineering and drug delivery biopolymers, *J. Drug Deliv. Sci. Technol.* 63 (2021), <https://doi.org/10.1016/j.jddst.2021.102431>.
- [11] D. Kumar, R.R. Pal, N. Das, P. Roy, S.A. Saraf, S. Bayram, P.P. Kundu, Synthesis of flaxseed gum/melanin-based scaffold: a novel approach for nano-encapsulation of doxorubicin with enhanced anticancer activity, *Int. J. Biol. Macromol.* 256 (2024), <https://doi.org/10.1016/j.ijbiomac.2023.127964>.
- [12] A. Plucinski, Z. Lyu, B.V.K.J. Schmidt, Polysaccharide nanoparticles: from fabrication to applications, *J. Mater. Chem. B* 9 (2021) 7030–7062, <https://doi.org/10.1039/dtb00628b>.
- [13] T. Miao, J. Wang, Y. Zeng, G. Liu, X. Chen, Polysaccharide-based controlled release systems for therapeutics delivery and tissue engineering: from bench to bedside, *Adv. Sci.* 5 (2018), <https://doi.org/10.1002/advs.201700513>.
- [14] A. Sood, A. Gupta, G. Agrawal, Recent advances in polysaccharides based biomaterials for drug delivery and tissue engineering applications, *Carbohydr. Polym. Technol. Appl.* 2 (2021), <https://doi.org/10.1016/j.carpta.2021.100067>.
- [15] H. Zong, B. Wang, G. Li, S. Yan, K. Zhang, Y. Shou, J. Yin, Biodegradable high-strength hydrogels with injectable performance based on poly(L-glutamic acid) and Gellan gum, *ACS Biomater. Sci. Eng.* 6 (2020) 4702–4713, <https://doi.org/10.1021/acsbiomaterials.0c00915>.
- [16] A. Astanina, J.T. Koivisto, M. Hannula, T. Salminen, M. Kellomäki, J. Massera, Chemical interactions in composites of gellan gum and bioactive glass: self-crosslinking and in vitro dissolution, *Front. Chem.* 11 (2023), <https://doi.org/10.3389/fchem.2023.1133374>.
- [17] H. Carrélo, A.R. Escoval, P.I.P. Soares, J.P. Borges, M.T. Cidade, Injectable composite systems of Gellan Gum:alginate microparticles in pluronic hydrogels for bioactive cargo controlled delivery: optimization of hydrogel composition based on rheological behavior, *Fluids* 7 (2022), <https://doi.org/10.3390/fluids7120375>.
- [18] S. in Kim, G.Y. Jeon, S.E. Kim, S.H. Choe, S.J. Kim, J.S. Seo, T.W. Kang, J.E. Song, G. Khang, Injectable hydrogel based on Gellan Gum/silk sericin for application as a retinal pigment epithelium cell carrier, *ACS Omega* 7 (2022) 41331–41340, <https://doi.org/10.1021/acsomega.2c05113>.
- [19] R.R. Bhosale, H.V. Gangadharappa, R.A.M. Osmani, D.V. Gowda, Design and development of polymethylmethacrylate-grafted gellan gum (PMMA-g-GG)-based pH-sensitive novel drug delivery system for antidiabetic therapy, *Drug Deliv. Transl. Res.* 10 (2020) 1002–1018, <https://doi.org/10.1007/s13346-020-00776-7>.
- [20] W. He, Y. Wu, Z. Luo, G. Yang, W. Ye, X. Chen, J. Ren, T. Liang, Z. Liao, S. Jiang, K. Wang, Injectable Decorin/Gellan gum hydrogel encapsulating adipose-derived stem cells enhances anti-inflammatory effect in cartilage injury via autophagy signaling, *Cell Transplant.* 32 (2023), <https://doi.org/10.1177/09636897231196493>.
- [21] F.B. Albrecht, V. Dolderer, S. Nellinger, F.F. Schmidt, P.J. Kluger, Gellan gum is a suitable biomaterial for manual and bioprinted setup of long-term stable, functional 3D-adipose tissue models, *Gels* 8 (2022), <https://doi.org/10.3390/gels8070420>.
- [22] H. Yang, M. Wang, Y. Huang, Q. Qiao, C. Zhao, M. Zhao, In vitro and in vivo evaluation of a novel mitomycin nanomicelle delivery system, *RSC Adv.* 9 (2019) 14708–14717, <https://doi.org/10.1039/c9ra02660f>.
- [23] R.Y. Cheung, A.M. Rauth, X. Yu Wu, X.Y. Wu, In Vivo Efficacy and Toxicity of Intratumorally Delivered Mitomycin C and Its Combination With Doxorubicin Using Microsphere Formulations, 2005, <https://doi.org/10.1097/00001813-200504000-00009>.
- [24] L. Lamch, K.A. Wilk, I. Déák, V. Hornok, L. Janovák, Rational mitomycin nanocarriers based on hydrophobically functionalized polyelectrolytes and poly(lactide-co-glycolide), *Langmuir* 38 (2022) 5404–5417, <https://doi.org/10.1021/acs.langmuir.1c03360>.
- [25] L. Lamch, K.A. Wilk, I. Déák, V. Hornok, L. Janovák, Rational mitomycin nanocarriers based on hydrophobically functionalized polyelectrolytes and poly(lactide-co-glycolide), *Langmuir* 38 (2022) 5404–5417, <https://doi.org/10.1021/acs.langmuir.1c03360>.
- [26] M. Manzano, A. Gabizón, M. Vallet-Regí, Characterization of a mesoporous silica nanoparticle formulation loaded with Mitomycin C Lipidic Prodrug (MLP) and in vitro comparison with a clinical-stage liposomal formulation of MLP, *Pharmaceutics* 14 (2022), <https://doi.org/10.3390/pharmaceutics14071483>.
- [27] H. Yang, M. Wang, Y. Huang, Q. Qiao, C. Zhao, M. Zhao, In vitro and in vivo evaluation of a novel mitomycin nanomicelle delivery system, *RSC Adv.* 9 (2019) 14708–14717, <https://doi.org/10.1039/c9ra02660f>.
- [28] Z. Hou, Y. Li, Y. Huang, C. Zhou, J. Lin, Y. Wang, F. Cui, S. Zhou, M. Jia, S. Ye, Q. Zhang, Phytosomes loaded with mitomycin C-soybean phosphatidylcholine complex developed for drug delivery, *Mol. Pharm.* 10 (2013) 90–101, <https://doi.org/10.1021/mp300489p>.
- [29] M. Wu, S. Wang, Y. Wang, F. Zhang, T. Shao, Targeted delivery of mitomycin C-loaded and LDL-conjugated mesoporous silica nanoparticles for inhibiting the proliferation of pterygium subconjunctival fibroblasts, *Exp. Eye Res.* 197 (2020), <https://doi.org/10.1016/j.exer.2020.108124>.
- [30] Q.M. Zhou, Y. Sun, Y.Y. Lu, H. Zhang, Q.L. Chen, S.B. Su, Curcumin reduces mitomycin C resistance in breast cancer stem cells by regulating Bcl-2 family-mediated apoptosis, *Cancer Cell Int.* 17 (2017), <https://doi.org/10.1186/s12935-017-0453-3>.
- [31] M. Razmi, A. Rabbani-Chadegani, F. Hashemi-Niasari, P. Ghadam, Lithium chloride attenuates mitomycin C induced necrotic cell death in MDA-MB-231 breast cancer cells via HMGB1 and Bax signaling, *J. Trace Elem. Med. Biol.* 48 (2018) 87–96, <https://doi.org/10.1016/j.jtemb.2018.03.011>.
- [32] Y. Patil, Y. Amitay, P. Ohana, H. Shmeeda, A. Gabizon, Targeting of pegylated liposomal mitomycin-C prodrug to the folate receptor of cancer cells: intracellular activation and enhanced cytotoxicity, *J. Control. Release* 225 (2016) 87–95, <https://doi.org/10.1016/j.jconrel.2016.01.039>.
- [33] V.T. Banala, S. Urandur, S. Sharma, M. Sharma, R.P. Shukla, D. Marwaha, S. Gautam, M. Dwivedi, P.R. Mishra, Targeted co-delivery of the aldose reductase inhibitor epalrestat and chemotherapeutic doxorubicin: via a redox-sensitive prodrug approach promotes synergistic tumor suppression, *Biomater. Sci.* 7 (2019) 2889–2906, <https://doi.org/10.1039/c9bm00221a>.
- [34] K. Soleimani, H. Derakhshankhah, M. Jaymand, H. Samadian, Stimuli-responsive natural gums-based drug delivery systems for cancer treatment, *Carbohydr. Polym.* 254 (2021), <https://doi.org/10.1016/j.carbpol.2020.117422>.
- [35] R.R. Pal, D. Kumar, V. Raj, V. Rajpal, P. Maurya, S. Singh, N. Mishra, N. Singh, P. Singh, N. Tiwari, S.A. Saraf, Synthesis of pH-sensitive crosslinked guar gum-g-poly(acrylic acid-co-acrylonitrile) for the delivery of thymoquinone against inflammation, *Int. J. Biol. Macromol.* 182 (2021) 1218–1228, <https://doi.org/10.1016/j.ijbiomac.2021.05.072>.
- [36] T. Bal, S.K. Yadav, N. Rai, S. Swain, S. Shambavi, G. Sen Garg, Invitro evaluations of free radical assisted microwave irradiated polyacrylamide grafted cashew gum (CG) biocompatible graft copolymer (CG-g-PAM) as effective polymeric scaffold, *J. Drug Deliv. Sci. Technol.* 56 (2020), <https://doi.org/10.1016/j.jddst.2020.101572>.

- [37] B.C. Thanoo, A. Jayakrishnan, Preparation of hydrogel beads from crosslinked poly (methyl methacrylate) microspheres by alkaline hydrolysis, *J. Appl. Polym. Sci.* 39 (1990) 1153–1161, <https://doi.org/10.1002/app.1990.070390510>.
- [38] D. Das, A. Roy, S. Pal, A polysaccharide-based pH-sensitive hybrid hydrogel as a sustained release matrix for antimicrobial drugs, *ACS Appl. Polym. Mater.* 5 (2023) 3348–3358, <https://doi.org/10.1021/acsappm.2c02256>.
- [39] S. Sharma, A. Verma, J. Singh, B.V. Teja, N. Mittapelly, G. Pandey, S. Urandur, R. P. Shukla, R. Konwar, P.R. Mishra, Vitamin B6 tethered endosomal pH responsive lipid nanoparticles for triggered intracellular release of doxorubicin, *ACS Appl. Mater. Interfaces* 8 (2016) 30407–30421, <https://doi.org/10.1021/acsami.6b08958>.
- [40] S. Verma, S.K. Singh, P.R.P. Verma, Fabrication of lipidic nanocarriers of loratadine for facilitated intestinal permeation using multivariate design approach, *Drug Dev. Ind. Pharm.* 42 (2016) 288–306, <https://doi.org/10.3109/03639045.2015.1052078>.
- [41] M. Kumari, S.K. Gupta, Response surface methodological (RSM) approach for optimizing the removal of trihalomethanes (THMs) and its precursor's by surfactant modified magnetic nanoadsorbents (sMNP) - an endeavor to diminish probable cancer risk, *Sci. Rep.* 9 (2019), <https://doi.org/10.1038/s41598-019-54902-8>.
- [42] P. Tiwari, R.P. Shukla, K. Yadav, N. Singh, D. Marwaha, S. Gautam, A.K. Bakshi, N. Rai, A. Kumar, D. Sharma, P.R. Mishra, Dacarbazine-primed carbon quantum dots coated with breast cancer cell-derived exosomes for improved breast cancer therapy, *J. Control. Release* 365 (2024) 43–59, <https://doi.org/10.1016/j.jconrel.2023.11.005>.
- [43] R. Jaryal, S.A. Khan, Liquid-assisted mechanochemical synthesis, crystallographic, theoretical and molecular docking study on HIV instosome of novel copper complexes: (μ -acetato)-bis(2,2'-bipyridine)-copper and bromidotetrakis(2-methyl-1H-imidazole)-copper bromide, *BioMetals* 36 (2023) 975–996, <https://doi.org/10.1007/s10534-023-00498-6>.
- [44] Saruchi, V. Kumar, H. Mittal, S. Ansar, Synthesis and characterization of Gellan gum-based hydrogels for the delivery of anticancer drug etoposide, *Int. J. Biol. Macromol.* 278 (2024), <https://doi.org/10.1016/j.ijbiomac.2024.135007>.
- [45] S. Gautam, N. Singh, D. Marwaha, N. Rai, M. Sharma, P. Tiwari, S. Singh, A. Kumar Bakshi, A. Kumar, N. Agarwal, R. Prakash Shukla, P. Ranjan Mishra, Celastrol-loaded polymeric mixed micelles shows improved antitumor efficacy in 4 T1 bearing xenograft mouse model through spatial targeting, *Int. J. Pharm.* 659 (2024), <https://doi.org/10.1016/j.ijipharm.2024.124234>.
- [46] X. Li, S. Yuan, K.J. Shea, G. Qiu, X. Lu, R. Zhang, Redox/temperature responsive nonionic nanogel and photonic crystal hydrogel: comparison between N, N'-Bis (acryloyl)cystamine and N, N'-methylenebisacrylamide, *Polymer (Guildf.)* 137 (2018) 112–121, <https://doi.org/10.1016/j.polymer.2017.12.066>.
- [47] H. Mahdiani, F. Yazdani, M. Khoramipour, V. Valizadeh, H. Bakhshandeh, R. Dinarvand, Preparation and physicochemical characterization of hyaluronic acid-lysine nanogels containing serratiopeptidase to control biofilm formation, *Sci. Rep.* 14 (2024), <https://doi.org/10.1038/s41598-024-56732-9>.
- [48] R. Saklani, P.K. Yadav, M.A. Nengroo, S.L. Gawali, P.A. Hassan, D. Datta, D. P. Mishra, I. Dierking, M.K. Chourasia, An injectable in situ depot-forming lipidic lyotropic liquid crystal system for localized intratumoral drug delivery, *Mol. Pharm.* 19 (2022) 831–842, <https://doi.org/10.1021/acs.molpharmaceut.1c00782>.
- [49] P. Dhamija, A.K. Mehata, R. Tamang, J. Bonlawar, N. Vaishali, A.K. Malik, A. Setia, S. Kumar, R.R. Challa, B. Koch, M.S. Muthu, Redox-sensitive poly(lactic-co-glycolic acid) nanoparticles of palbociclib: development, ultrasound/photoacoustic imaging, and smart breast cancer therapy, *Mol. Pharm.* 21 (2024) 2713–2726, <https://doi.org/10.1021/acs.molpharmaceut.3c01086>.
- [50] M. Sharma, N. Mittapelly, V.T. Banala, S. Urandur, S. Gautam, D. Marwaha, N. Rai, N. Singh, A. Gupta, K. Mitra, P.R. Mishra, Amalgamated microneedle array bearing ribociclib-loaded transfosomes eradicates breast cancer via CD44 targeting, *Biomacromolecules* 23 (2022) 661–675, <https://doi.org/10.1021/acs.biomac.1c01076>.
- [51] S. Yang, J.J. Zhang, X.Y. Huang, Mouse models for tumor metastasis, *Methods Mol. Biol.* 928 (2012) 221–228, https://doi.org/10.1007/978-1-62703-008-3_17.
- [52] X. Peng, G. Yang, Y. Shi, Y. Zhou, M. Zhang, S. Li, Box–Behnken design based statistical modeling for the extraction and physicochemical properties of pectin from sunflower heads and the comparison with commercial low-methoxyl pectin, *Sci. Rep.* 10 (2020), <https://doi.org/10.1038/s41598-020-60339-1>.
- [53] R.R. Bhosale, R.A.M. Osmani, A.S. Abu Lila, E.S. Khafagy, H.H. Arab, D.V. Gowda, M. Rahamathulla, U. Hani, M. Adnan, H.V. Gangadharappa, Ghatti gum-base graft copolymer: a plausible platform for pH-controlled delivery of antidiabetic drugs, *RSC Adv.* 11 (2021) 14871–14882, <https://doi.org/10.1039/d1ra01536b>.
- [54] R.K. Sharma, Lalita, Synthesis and characterization of graft copolymers of N-Vinyl-2-Pyrrolidone onto guar gum for sorption of Fe²⁺ and Cr⁶⁺ ions, *Carbohydr. Polym.* 83 (2011) 1929–1936, <https://doi.org/10.1016/j.carbpol.2010.10.068>.
- [55] S.H. Jung, S. Schneider, F. Plamper, A. Pich, Responsive supramolecular microgels with redox-triggered cleavable crosslinks, *Macromolecules* 53 (2020) 1043–1053, <https://doi.org/10.1021/acs.macromol.9b01292>.
- [56] S.A. Algharib, A. Dawood, K. Zhou, D. Chen, C. Li, K. Meng, M.K. Ma, S. Ahmed, L. Huang, S. Xie, Designing, structural determination and biological effects of rifaximin loaded chitosan- carboxymethyl chitosan nanogel, *Carbohydr. Polym.* 248 (2020), <https://doi.org/10.1016/j.carbpol.2020.116782>.
- [57] A. Dinari, M. Abdollahi, M. Sadeghizadeh, Design and fabrication of dual responsive lignin-based nanogel via “grafting from” atom transfer radical polymerization for curcumin loading and release, *Sci. Rep.* 11 (2021), <https://doi.org/10.1038/s41598-021-81393-3>.
- [58] S. Tang, Z. Shi, Y. Cao, W. He, Facile aqueous-phase synthesis of multi-responsive nanogels based on polyetheramines and bisepoxide, *J. Mater. Chem. B* 1 (2013) 1628–1634, <https://doi.org/10.1039/c3tb00492a>.
- [59] A.H. Pandit, S. Nisar, K. Imtiyaz, M. Nadeem, N. Mazumdar, M.M.A. Rizvi, S. Ahmad, Injectable, self-healing, and biocompatible N,O-carboxymethyl chitosan/multialdehyde guar gum hydrogels for sustained anticancer drug delivery, *Biomacromolecules* 22 (2021) 3731–3745, <https://doi.org/10.1021/acs.biomac.1c00537>.
- [60] A. Kumar, Deepak, S. Sharma, A. Srivastava, R. Kumar, Synthesis of xanthan gum graft copolymer and its application for controlled release of highly water soluble Levofloxacin drug in aqueous medium, *Carbohydr. Polym.* 171 (2017) 211–219, <https://doi.org/10.1016/j.carbpol.2017.05.010>.
- [61] S.K. Filippov, R. Khusnutdinov, A. Murniliuk, W. Inam, L.Y. Zakharchova, H. Zhang, V.V. Khutoryanskiy, Dynamic light scattering and transmission electron microscopy in drug delivery: a roadmap for correct characterization of nanoparticles and interpretation of results, *Mater. Horiz.* 10 (2023) 5354–5370, <https://doi.org/10.1039/d3mh00717k>.
- [62] Z. Liu, P. Yao, Injectable thermo-responsive hydrogel composed of xanthan gum and methylcellulose double networks with shear-thinning property, *Carbohydr. Polym.* 132 (2015) 490–498, <https://doi.org/10.1016/j.carbpol.2015.06.013>.
- [63] M.H. Chen, L.L. Wang, J.J. Chung, Y.H. Kim, P. Atluri, J.A. Burdick, Methods to assess shear-thinning hydrogels for application as injectable biomaterials, *ACS Biomater. Sci. Eng.* 3 (2017) 3146–3160, <https://doi.org/10.1021/acsbiomaterials.7b00734>.
- [64] C. Modrogan, A.M. Pandele, C. Bobirică, D. Dobrotă, A.M. Dăncilă, G. Gărleanu, O. D. Orbuț, C. Borda, D. Gărleanu, C. Orbeci, Synthesis, characterization and sorption capacity examination for a novel hydrogel composite based on gellan gum and graphene oxide (GG/GO), *Polymers (Basel)* 12 (2020), <https://doi.org/10.3390/POLYM12051182>.
- [65] S. Choudhary, K. Sharma, M.S. Bhatti, V. Sharma, V. Kumar, DOE-based synthesis of gellan gum-acrylic acid-based biodegradable hydrogels: screening of significant process variables and in situ field studies, *RSC Adv.* 12 (2022) 4780–4794, <https://doi.org/10.1039/d1ra08786j>.
- [66] D.F. Coutinho, S.V. Sant, H. Shin, J.T. Oliveira, M.E. Gomes, N.M. Neves, A. Khademhosseini, R.L. Reis, Modified Gellan Gum hydrogels with tunable physical and mechanical properties, *Biomaterials* 31 (2010) 7494–7502, <https://doi.org/10.1016/j.biomaterials.2010.06.035>.
- [67] L.E. Agibayeva, D.B. Kaldybekov, N.N. Porfirjeva, V.R. Garipova, R. A. Mangabayeva, R.I. Moustafine, I.I. Semina, G.A. Mun, S.E. Kudaibergenov, V. V. Khutoryanskiy, Gellan gum and its methacrylated derivatives as in situ gelling mucoadhesive formulations of pilocarpine: in vitro and in vivo studies, *Int. J. Pharm.* 577 (2020), <https://doi.org/10.1016/j.ijipharm.2020.119093>.
- [68] R.R. Bhosale, H.V. Gangadharappa, R.A.M. Osmani, D.V. Gowda, Design and development of polymethylmethacrylate-grafted gellan gum (PMMA-g-GG)-based pH-sensitive novel drug delivery system for antidiabetic therapy, *Drug Deliv. Transl. Res.* 10 (2020) 1002–1018, <https://doi.org/10.1007/s13346-020-00776-7>.
- [69] R.R. Bhosale, R.A.M. Osmani, A.S. Abu Lila, E.S. Khafagy, H.H. Arab, D.V. Gowda, M. Rahamathulla, U. Hani, M. Adnan, H.V. Gangadharappa, Ghatti gum-base graft copolymer: a plausible platform for pH-controlled delivery of antidiabetic drugs, *RSC Adv.* 11 (2021) 14871–14882, <https://doi.org/10.1039/d1ra01536b>.
- [70] S. Sharma, T. Bal, Exploring and characterizing the drug release potential of novel tissue compatible amphiphilic graft copolymer of polyvinyl acetate grafted neem gum (NG-g-PVAc), *J. Polym. Environ.* 31 (2023) 2364–2379, <https://doi.org/10.1007/s10924-023-02765-6>.
- [71] H. Yang, M. Wang, Y. Huang, Q. Qiao, C. Zhao, M. Zhao, In vitro and in vivo evaluation of a novel mitomycin nanomicelle delivery system, *RSC Adv.* 9 (2019) 14708–14717, <https://doi.org/10.1039/c9ra02660f>.
- [72] C. Cottet-Rousselle, X. Ronot, X. Leverve, J.F. Mayol, Cytometric assessment of mitochondria using fluorescent probes, *Cytometry A* 79 (A) (2011) 405–425, <https://doi.org/10.1002/cyto.a.21061>.
- [73] Y. Zhang, P. Dosta, J. Conde, N. Oliva, M. Wang, N. Artzi, Prolonged local in vivo delivery of stimuli-responsive nanogels that rapidly release doxorubicin in triple-negative breast cancer cells, *Adv. Healthc. Mater.* 9 (2020), <https://doi.org/10.1002/adhm.201901101>.
- [74] K. Asif, M. Adeel, M.M. Rahman, I. Caligiuri, T. Perin, M. Cemazar, V. Canzonieri, F. Rizzolio, Iron nitroprusside as a chemodynamic agent and inducer of ferroptosis for ovarian cancer therapy, *J. Mater. Chem. B* 11 (2023) 3124–3135, <https://doi.org/10.1039/d2tb02691k>.
- [75] W. Wu, H. Chen, F. Shan, J. Zhou, X. Sun, L. Zhang, T. Gong, A novel doxorubicin-loaded in situ forming gel based high concentration of phospholipid for intratumoral drug delivery, *Mol. Pharm.* 11 (2014) 3378–3385, <https://doi.org/10.1021/mp500019p>.
- [76] T. Wang, J. Meng, C. Wang, T. Wen, M. Jia, Y. Ge, L. Xie, S. Hao, J. Liu, H. Xu, Inhibition of murine breast cancer metastases by hydrophilic As4S4 nanoparticles is associated with decreased ROS and HIF-1 α downregulation, *Front. Oncol.* 9 (2019), <https://doi.org/10.3389/fonc.2019.00333>.
- [77] A. Mishra, M. Bano, A.C. Bisen, S. Verma, S.N. Sanap, R. Kishor, P.K. Shukla, R. S. Bhatta, Topical corneal targeted sustained release amphotericin B liposomal formulation for the treatment of fungal keratitis and its PK-PD evaluation, *J. Drug Deliv. Sci. Technol.* 60 (2020), <https://doi.org/10.1016/j.jddst.2020.101944>.